

ACOUSTIC MONITORING OF HYDRAULIC STIMULATION IN GRANITES

by
John Calvin hood

Copyright by John Calvin Hood 2014

All Rights Reserved

A thesis submitted to the Faculty and the Board of Trustees of the Colorado School of Mines in partial fulfillment of the requirements for the degree of Masters of Science (Civil Engineering).

Golden, Colorado

Date _____

Signed: _____
John Calvin Hood
Student Name

Signed: _____
Dr. Marte Gutierrez
Thesis Adviser

Signed: _____
Dr. Mike Mooney
Thesis Committee

Signed: _____
Dr. André Revil
Thesis Committee

Golden, Colorado

Date _____

Signed: _____
Dr. John McCray
Program Head

ACKNOWLEDGMENTS

I would like to thank my adviser Dr. Marte Gutierrez and committee members Dr. Mike Mooney and Dr. Révil for all of their time and dedication. I would also like to thank my lab partner Luke Frash and my predecessor Jesse Hampton for all of their hard work and assistance both inside and outside the lab. Lastly, I would like to thank my friends and family for their patience during these last two years. This work would not have been possible without their love and support.

ABSTRACT

Enhanced Geothermal Systems (EGS) have substantial potential as a domestic energy source and is well suited as an alternative to diversify the national energy portfolio due to its high levels of heat and recoverable energy. Hydraulic fracture stimulation of low permeability EGS reservoir rock is widely employed to develop this resource and is generally required to make unconventional resources an economically viable resource. Significant challenges for EGS technology include poor connectivity between injection and production wells during stimulation and difficulty predicting fracture growth (Tester, et al. 2006). This, coupled with notable advances in oil and gas recovery, has made hydraulic fracture mechanics the subject of considerable study.

Acoustic emissions, or microseisms, contribute greatly to these studies and have been employed on a wide range of topics in rock mechanic studies. At Colorado School of Mines, acoustic emission technology has been employed to monitor stimulation of cubic granite samples under heated and true triaxial stress environments to simulate deep reservoir conditions. Recorded AE activity was used to determine proper location of production well placement while additional analysis on the fracture process using characteristics such as wave amplitude and hit rates were used to identify stages of activity during fracture propagation. Study of the spatial and time dependence of the initiation and growth of rock fractures is critical to understanding the processes that govern fracture behavior and require details that are not accessible to alternative methods of analysis. Acoustic emissions can provide crucial information and represent an important part of rock mechanics studies.

TABLE OF CONTENTS

Abstract	iv
Table of Contents	v
List of Figures	vii
List of Tables	x
1. Introduction	1
1.1. Literature review	1
1.1.1. Acoustic Characteristics	2
1.1.2. Fracture Geometry	4
1.1.3. Focal Mechanisms	7
1.2. Background	11
1.3. Motivations	14
1.4. Objectives	14
2. Methodology	16
2.1. Test equipment	16
2.1.1. Injection Fluid	18
2.1.2. AEwin and software	18
2.1.3. Test Materials	21
3. Test Results and Data	23
3.1. Sample G01-91	23
3.1.1. Pressure and Acoustics	25

3.1.2.	<i>Pressure and Strain</i>	28
3.1.3.	<i>Strain and Acoustics</i>	29
3.1.4.	<i>Geometry</i>	31
3.2.	Sample G01-92.....	35
3.2.1.	<i>High Initial Permeability</i>	38
3.2.2.	<i>Pressure, Strain, and Acoustics</i>	39
3.2.3.	<i>Fracture Geometry</i>	45
3.3.	Sample G01-93.....	46
3.3.1.	Acoustics and Pressure	48
3.3.2.	<i>Fracture Geometry</i>	51
3.3.3.	Post Stimulation Flow	54
4.	Summary and ConclusionS.....	58
4.1.	Summary	58
4.2.	Conclusions	58
4.3.	Recommendations for Future Studies	61
5.	Appendix	62
6.	Works Cited.....	63

LIST OF FIGURES

FIGURE 1: CONVENTIONAL BREAKDOWN PRESSURE CURVE	2
FIGURE 2: MODES OF FAILURE. BLACK ARROWS REPRESENT DIRECTION OF MOTION AND RED ARROWS REPRESENT FRACTURE SURFACE DIRECTION.	9
FIGURE 3: SIMPLE DIAGRAM OF THE TRIAXIAL CELL AND ITS FUNDAMENTAL COMPONENTS.	17
FIGURE 4: IMAGE OF A LOADED SAMPLE INSIDE THE TRIAXIAL CELL (LEFT) AND DUAL PUMP INJECTION SYSTEM (RIGHT).	17
FIGURE 5: PLATEN, ACOUSTIC SENSOR WITH PREAMPLIFIER, FOAM SLEEVE AND BACKING.....	19
FIGURE 6: IDEALIZED WAVEFORM FOR COMPONENT DESCRIPTION (PAC 2007)	21
FIGURE 7: SAMPLE G01-93 WITH SENSORS ATTACHED.....	21
FIGURE 8: LOCATION OF STRAIN GAUGES AND ACOUSTIC SENSORS ON SAMPLE G01-91.	24
FIGURE 9: PRESSURE AND HIT ACTIVITY IN ONE SECOND BINS FOR THE DURATION OF STIMULATION.	26
FIGURE 10: WINDOW OF THE STIMULATION TIME INTERVAL AT 5000-5600 SECONDS (HIGHLIGHTED IN FIGURE 9). SEVERAL STAGES OF FRACTURE CAN BE IDENTIFIED THROUGH CHANGES TO PRESSURE AND HIT COUNTS.	27
FIGURE 11: PRESSURE AND AMPLITUDE SPREAD FOR SAMPLE G01-91 AT 5000-5600 SECONDS (HIGHLIGHTED IN FIGURE 9). HIT COUNTS ARE PLOTTED RELATIVE TO PRESSURE, WITH MAX HIT RATE EQUIVALENT TO MAX PRESSURE.	27
FIGURE 12: PRESSURE AND STRAIN READINGS FROM 5000 TO 5600 SECONDS FOR SAMPLE G01-91. NOTE THE DISTINCT VARIATION IN STRAIN FOR THE FOUR DIFFERENT GAUGES.	29
FIGURE 13: ACOUSTIC HIT COUNT AND STRAIN BETWEEN 5000 AND 5600 SECONDS GRAPHED TOGETHER FOR SAMPLE G01-91. PRESSURE SCALED RELATIVE TO HIT COUNTS	30
FIGURE 14: STRAIN GAUGES AND B-VALUE FROM 5000 TO 5600 SECONDS GRAPHED TOGETHER FOR SAMPLE G01-91. STRAIN GAUGE 6 FAILED WHERE THE LINE GOES VERTICAL.	31

FIGURE 15: ESTIMATE OF FRACTURE LOCATION FROM ALL EVENTS IN SAMPLE G01-91. EVENTS LOCATIONS ARE RELATIVE TO A THEORETICAL PLANE ROTATED THROUGH THE POSITIVE X-AXIS.	32
FIGURE 16: STAGE 1 EVENTS.....	33
FIGURE 17: TOP VIEW OF SAMPLE G01-91. NOTE THE BAND OF COARSER CRYSTALLINE MATERIAL RUNNING DIAGONALLY ACROSS THE MIDDLE OF THE SAMPLE FROM LEFT TO RIGHT.	34
FIGURE 18: STAGE 3 EVENTS.....	34
FIGURE 19: G01-92 LOADED SAMPLE AMPLITUDE MEASUREMENTS	37
FIGURE 20: G01-92 STRAIN GAUGE LAYOUT	38
FIGURE 21: G01-92 PUMP-A FLUID VOLUME DURING INITIAL 2 MPA CP INTERVAL.....	39
FIGURE 22: PRESSURE AND LOG COUNT OF HIT RATES FOR THE FIRST SET OF STIMULATION TRIALS	40
FIGURE 23: WELL PRESSURE AND A LOG COUNT OF ACOUSTIC ACTIVITY FOR STAGES 2, 3, AND 4 ...	41
FIGURE 24: PLOT OF HIT ACTIVITY REACTIVATION STRESS AGAINST PREVIOUS MAXIMUM STRESS. STAGE 3 IS EXCLUDED FROM THE TREND ANALYSIS BECAUSE OF ITS LOW LEVEL OF ACTIVITY. ...	41
FIGURE 25: HIT COUNT AT THE TIME OF BREAKDOWN USING A CONSTANT FLOW OF 1.6 ML/MIN	42
FIGURE 26: LOCATION OF SENSORS AND AREA OF FRACTURE DETECTION	43
FIGURE 27: LOGARITHMIC HIT COUNTS WITH PRESSURE AND STRAIN AT TWO GAUGES LOCATED ON PERPENDICULAR FACES. HIT COUNTS ARE NORMALIZED RELATIVE TO PRESSURE. HITS INCREASE AT 29220 SECONDS AND FALL AGAIN AT 29230.....	44
FIGURE 28: CHANGE IN THE AMPLITUDE SPREAD WITH TIME AND PRESSURE. THE TRUE AMPLITUDES ARE NORMALIZED AND SCALED AGAINST PRESSURE. THE AMPLITUDES RANGE BETWEEN 25 dB (THRESHOLD) AND 66 dB (MAX DETECTED).	44
FIGURE 29: (LEFT) EVENTS AT BREAKDOWN (RIGHT) ALL EVENTS,	46
FIGURE 30: EXAMPLE OF ANGLED INJECTION WELL (WHITE) WITH APPROXIMATE DEPTH DIMENSIONS	47
FIGURE 31: PLOT OF OUT OF CELL ATTENUATION AND IN CELL ATTENUATION FOR G01-93,.....	48
FIGURE 32: HIT COUNT HISTOGRAM OF STIMULATION ONE PLOTTED WITH PRESSURE	49

FIGURE 33: LOG-SCALED HIT HISTOGRAM FROM THE FIRST RE-STIMULATION TEST.	51
FIGURE 34: PRESSURE FROM CONSTANT FLOW TESTS. FLOW BETWEEN $2.27 - 2.29 \times 10^6$ SEC IS 6.4 ML/MIN. THE LEFT ARROW SHOWS PRESSURE SPIKE DUE TO PUMP CHANGE AND THE RIGHT ARROW SHOW THE TIME WHEN DYE WAS ADDED TO THE INJECTION FLUID.	51
FIGURE 35: FILTERED EVENT LOCATIONS.....	53
FIGURE 36: CENTERED TOP – DENSITY FOR ALL FILTERED EVENTS. BOTTOM LEFT – DENSITY FOR FILTERED EVENTS AT BREAKDOWN. BOTTOM RIGHT – DENSITY FOR FILTERED EVENTS PRIOR TO BREAKDOWN	53
FIGURE 37: PRODUCTION WELL PLACEMENT USING EVENT DENSITIES TO ESTIMATE FRACTURE GEOMETRY	55
FIGURE 38: SLICE 1, 2, AND 3 OF THE PLOTTED DISCONTINUITY BAND. THE CENTER CONTAINS PRODUCTION WELL INTERCEPTION.	56
FIGURE 39: PLOT OF EVENTS WITH DISCONTINUITY ENVELOPE. SLICE 1 (TOP) IS COLORED GREEN, SLICE 2 (MIDDLE) IS BLUE, AND SLICE 3 (BOTTOM) IS RED. LOCATIONS ARE NEAR THE DISCONTINUITY.	56
FIGURE 40: ALL STRAIN GAUGES FOR G01-91	62
FIGURE 41: ACOUSTIC HIT COUNTS AND PRESSURE DERIVATIVES AT BREAKDOWN. MAXIMUM PRESSURE CHANGE EXCEEDED THE CHARGE SCALE BY A FACTOR OF 8, REACHING NEARLY -6.5 MPA IN THE TERTIARY STAGE.	62

LIST OF TABLES

Table 1: Acoustic sensor characteristics	19
Table 2: Typical Colorado Red Rose granite characteristics	22
Table 3: List of sample acoustic properties	37
Table 4: List of G01-93 acoustic properties	48

1. INTRODUCTION

1.1. Literature review

Energy resources for electricity, transportation, heat, and the wide range of additional uses are of considerable importance as global energy consumption continues to increase. As a result, expanding the national energy portfolio to include a diverse collection of energy resources is critical to meet these demands. Geothermal energy has significant potential to contribute toward this goal owing to its vast domestic supply. Tester, et al. (2006) evaluated the technological and financial prospects of accessing geothermal resources and estimated potential resources between $200 - 600 \times 10^{21}$ joules. This represents as much as five thousand times the total energy consumption for the United States in 2011 (U.S. EIA, 2012). Geothermal power utilizes the earth's natural temperature gradient and ability to store heat as a tool for extracting energy resources. Ideally geothermal resources would circulate local fluids through naturally fractured, hot, permeable reservoir rock in order to produce heated steam for electricity production and hot water for other needs. When ideal conditions are unmet, however, reservoir properties may need to be enhanced to improve production efficiency. These stimulated reservoirs are known as Enhanced Geothermal Systems (EGS). Many EGS sites around the world have attempted to improve reservoir conditions by stimulating the host rock using hydraulic fracturing practices (Sasaki 1998; Haring, et al. 2008; Albright and Pearson 1982). Hydraulic fracture stimulation opens new fractures or activates existing fracture networks by injecting high-pressure fluids through the rock matrix. Fracture will initiate once well pressure overcomes *in situ* field stresses and the rock strength. This characteristic onset pressure is termed breakdown pressure (Zoback, et al. 1977). Often pressure will decline as fractures open or extend and resistance to fluid flow decreases (Figure 1).

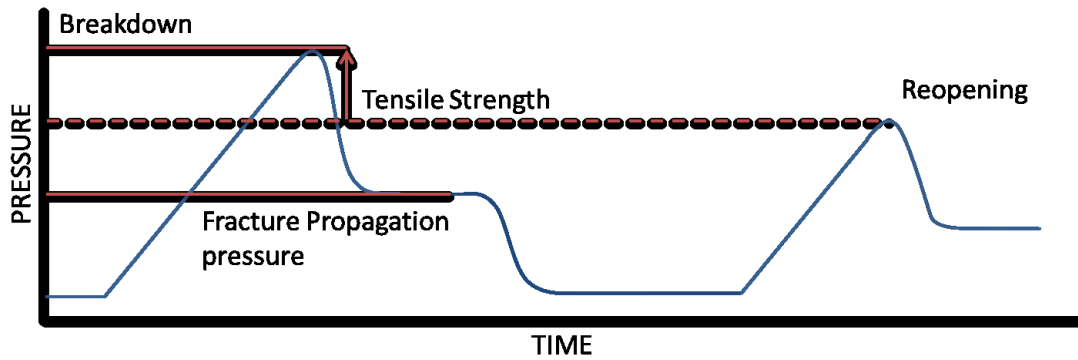


Figure 1: Conventional breakdown pressure curve

While many factors impact the commercial viability of EGS resources, fracture density and location are particularly significant and represents an active area of study. Under certain conditions, fracture density may have a linear relationship with net production, irrespective of production geometry (e.g., Sanyal and Butler 2005). In addition to improved fluid flow, stimulation of an EGS reservoir should also maximize fluid contact with the rockmass and provide time for heat lost to injection fluids to be recovered. Optimizing the rock-fluid interaction during development requires a robust understanding of the response of the reservoir to hydraulic stimulation. Difficulty in predicting formation response to hydraulic stimulation, growth of fracture networks and fracture densities, and direction or orientation of fracture propagation represents a significant challenge for EGS resources (e.g., Tester, et al. 2006). As a result, many sites have included microseismic emission monitoring systems to aid in the characterization and quality assessment of EGS reservoirs.

1.1.1. Acoustic Characteristics

Acoustic emission monitoring is a nondestructive monitoring technique used in laboratory and field environments to study material response under various load conditions through detection of elastic waves (Lockner, 1993; Ohtsu, et al., 1998; Shiotani, et al., 2001; Kao et al., 2011). These waves result from an extensive range of inter-granular activity that includes grain movements, surface sliding, fracture extension, stress buildup, and fluid flow

within the material being studied (Michlmayr et al., 2011; Shuck and Keech, 1975). Detected AE events can be analyzed to find global activity through acoustic count rates, damage zones through source location, as well as failure modes using several types of mechanism identification methods.

Early analysis of global activity studied amplitude distributions and their dependence on material type and method of failure. Pollock (1973) provides a brief interpretation of amplitude distributions and explores the possibility of using it as a precursor to failure. As a material is loaded under stress it deforms and stores this energy in its matrix. However, when stress exceeds the strength of a portion of the material it will fracture and release part of this as an acoustic wave. The energy released, and therefore the magnitude of measured amplitudes, has been shown to be proportional to the size of the displacements resulting from fracture (Pollock 1973). It was also suggested amplitude distribution would change during the loading process and could be a descriptor for stages of failure modes in composites or predictive measure when examining the ultimate strength of a material. However, this correlation is less detectable in materials that fail in a predominately ductile manner. While most of Pollock's studies examined steels, Mogi (1962) and Scholz (1968) both studied similar processes with respect to brittle failure of rock and reviewed possible correlations to earthquakes.

Mogi demonstrated that the degree of heterogeneity (material property) played a significant role in the amplitude distribution through flexural beam tests and a compression test on a range of materials. Heterogeneous materials, when stressed, will produce stress concentration due to irregularities and discontinuities associated with the varied components, their irregular shapes, and unequal strengths. When these concentrations reach local material strength it causes fracture. However, the same components will act as a barrier and prevent large fracture growth throughout the sample. The probability of small fracture creation is much greater than large fracture creation, and amplitude is comparable to displacement. Thus, the

chance for low amplitude activity is much larger than for high amplitude activity and the distribution represents the ratio of large fracture creation to small. Scholz (1968) added to these studies by demonstrating the stress dependence of micro-fracture development in samples through a variety of confining pressures during triaxial compression tests. The relationship describing this distribution has been described by Ishimoto and Iida (1939), Gutenberg and Richter (1944); and Aki (1965), and many others where the number of detections falling within an amplitude range is a log-log linear function.

For seismological and acoustic emission study, the slope of the line has been termed the b-value. In general, this relationship describes the ratio of high magnitude events relative to low magnitude events and can physically describe the state of fracture in a sample. Several recent studies (Rao and Lakshmi 2006, Rao and Lakshmi 2005, Aggelis, et al. 2011, Shiotani, Ohtsu and Ikeda 2001) examined this change in traditional and steel fiber reinforced concrete under flexural load and granites under uniaxial compression. Their work provided additional evidence to support the physical representation of b-value changes in a sample as increasing loads induced larger fractures.

1.1.2. Fracture Geometry

Fracture geometry, source location and real-time reservoir response are other important roles for acoustic monitoring technology. As discussed earlier, accurate source location is needed for geothermal reservoirs in order to properly align production wells in areas of high stimulation. Stimulation is also used for development of many oil and gas reservoirs. Warpinski (1998) examined the ability of acoustic technology to accurately measure dimensions of fractures created during stimulation. Additional studies provided insights into the effect of fluid viscosity on fracture growth using acoustic technology to map events (Warpinski, et al. 1998; Fisher, et al. 2001; Ishida, et al. 2004; Ishida, et al. 2012). These studies showed that fluids with lower viscosity tend to produce acoustic clouds and fracture networks that cover notably

larger areas than produced by more viscous fluids. In addition, the lengths of viscous clouds tend to be proportional to their heights. These observations suggest that low-viscosity fluids are capable of penetrating smaller imperfections in the rock matrices and permeate more quickly into formations. In contrast, more viscous fluids do not infiltrate the surrounding environment as quickly and tend to produce much wider and planar fractures. Laboratory and field experiments continue to provide significant insight into the effects of viscosity on network growth. Accurate description of how sample characteristics affect acoustic signals is important in order to reliably detect source locations for enhanced analysis of fracture geometry. Among the various factors, accurate velocity and acoustic attenuation profiles are particularly significant. Attenuation, or signal damping, is important because it distorts waveforms and actively limits detection distances. Common components of inelastic attenuation include permanent deformations, frictional sliding, and fluid filled pore networks (Stein and Wysession, 2002; Walsh, 1966). Review of several studies by Johnston et al. (1979) showed that for dry rock attenuation tends to be independent of frequency. Walsh (1966) showed that for surface waves attenuation held to approximately 400 kc/s (kHz). When fluids are introduced, the dependence of attenuation on frequency becomes considerable. In addition, higher confining pressure decreases attenuation due to closure of micro fractures present in geologic materials (Johnston, et al. 1979). Because attenuation limits the effective distance of an array relative to source locations (Warpinski, et al 1998; Michlmayr 2012), studies of fracture geometry require an understanding of the rate of decay in order to estimate the detectable distances available when optimizing locations of monitoring arrays. Wave velocities are also affected by the heterogeneous nature of rock. For seismic studies on both hydrocarbon and geothermal reservoirs, rock heterogeneity can significantly impact arrival time measurements and thus source location error. These effects can be mitigated using waveform tomography to improve results.

A variety of source location models have been adopted for acoustic emissions in order to locate sources through wave detection at sensors. Two commonly used models are the Geiger method and the Simplex method. The Geiger (1910, 1912) method has been traditionally used by seismologist for earthquake studies, and adaptations such as the Double Difference method (Waldhauser 2000) have been proposed to enhance location accuracy. Iterative approaches such as the Geiger method use derivative analysis to calculate an arrival time and compare the calculated value to observed data. The difference between the calculated and measured arrival times is then used to recalculate a source. However, a variety of unresolved factors associated with geologic materials can produce error in recorded times that will ultimately reduce the accuracy of the calculated location. The Double Difference method works on the initial source locations by determining locations based on spatial difference between source pairs, rather than source and sensor pairs. This approach improves accuracy by reducing the influence of variations in geologic material. The Simplex method (Prugger and Gendzwill 1988) uses the Nelder-Mead method of minimization to produce estimates. A variety of locations are provided to the Simplex algorithm and arrival times are estimated for each. The location that provides the highest error is removed from the initial simplex and given a new location. Each iteration removes the location estimate with the highest error and replaces it with a new source based on specified criteria until all sources begin to focus on a point. The geometric center of the resulting estimates is taken as the source location. The Prugger and Gendzwill (1988) adaptation of the Simplex method has been shown to benefit from the iterative approach because it is not susceptible to divergence like a derivative approach (Ge 2003).

An important factor in producing such errors for geologic materials is inelasticity and anisotropy produced from existing fractures and heterogeneity. Comprehensive studies have demonstrated that fractures are preferentially oriented as a result of *in situ* stresses (Hall, et al 2002; Bates, et al 1999; Winterstein 1992). The preferential orientation impacts body wave

velocities and thus can be used to characterize potential preferences in permeability. For fracture geometries, fractures can greatly impact source location estimates. Lockner, et al (1977), O'Connell and Budiansky (1974), and Benson, et al (2007) conducted laboratory experimentation that demonstrated the influence of external stresses (confinement, temperature) has on acoustic velocities. As confining stresses increase, fracture networks close and velocities increase. In contrast, increasing deviatoric stresses result in a drop of wave velocity attributable to opening old or creating new fractures.

For acoustic studies these anisotropies can have a notable influence on reservoir growth as well as source location estimates. The effects of inelasticity and anisotropy have been shown to have important impacts on fracture geometry by impacting both the physical fracture process and error influences associated with various techniques. Understanding how these factors can influence acoustic properties will improve assessment of fractures through proper velocity and attenuation modeling and lead to greater confidence in source location for fracture geometry estimation.

1.1.3. Focal Mechanisms

Focal mechanisms are an important part of microseismic and laboratory acoustic emission studies because they provide additional information on local failure mechanisms associated with global fracture development. Some characteristics obtained from focal mechanisms are displacement processes (tensile vs. shear) and fracture orientation. Proper understanding of micro cracking processes provides information about the effectiveness of stimulation techniques for optimal stimulation designs.

Rock mechanics theory describes three possible modes of failure depending on the type of displacement (Whittaker, et al. 1992). Failure modes depend on the orientation of fracture surface direction relative to surface movement (Figure 2). Mode I failure (tensile) is characterized by movements parallel to surface normal. Mode II and III failure (shear) is

characterized by surface movement perpendicular to the fracture surface normal. Mode III failure is characterized by a tearing motion with displacement normal to the fracture surface and that of mode II. This would be represented by movement into and out of the page. Pure modal failures are not necessarily experienced in granular, heterogeneous material due to random orientations of Griffith flaws and irregular stress concentrations. As such, failure modes comprising both tensile and shear (I-II and I-III) need to be considered as well. Rock mechanics theory describes hydraulic fracture generation as a tensile failure in which injected fluid pressurizes the rock matrix enough to overcome *in situ* confining stress based and matrix tensile strength. Early studies utilized this relationship to produce fracture prediction models based on tensile mechanics in order to predict lengths and widths of fractures under various fluid viscosity and environmental conditions (Daniel and White, 1980). Initially researchers using microseismic to monitor fracture location and geometry attempted to apply seismological techniques to determine focal mechanisms from the recorded waveforms. Despite the tensile nature of hydraulic fracture extension, field studies have shown repeatedly that recorded microseismic events are a result of shear failure likely caused by slip on natural fracture planes weakened by pore pressure changes (Wohlenberg and Keppler, 1987; Sleaf, et al. 1995; Warpinski, et al. 1998). As a result of this contradiction between theory and observations, many researchers have attempted to produce models based on shear fracture criteria. This observed ambiguity in theory reaffirming the need for more comprehensive understanding of the micro cracking process relative to the growth of hydraulic fractures (Maxwell, 2011; Taleghani and Lorenzo, 2011).

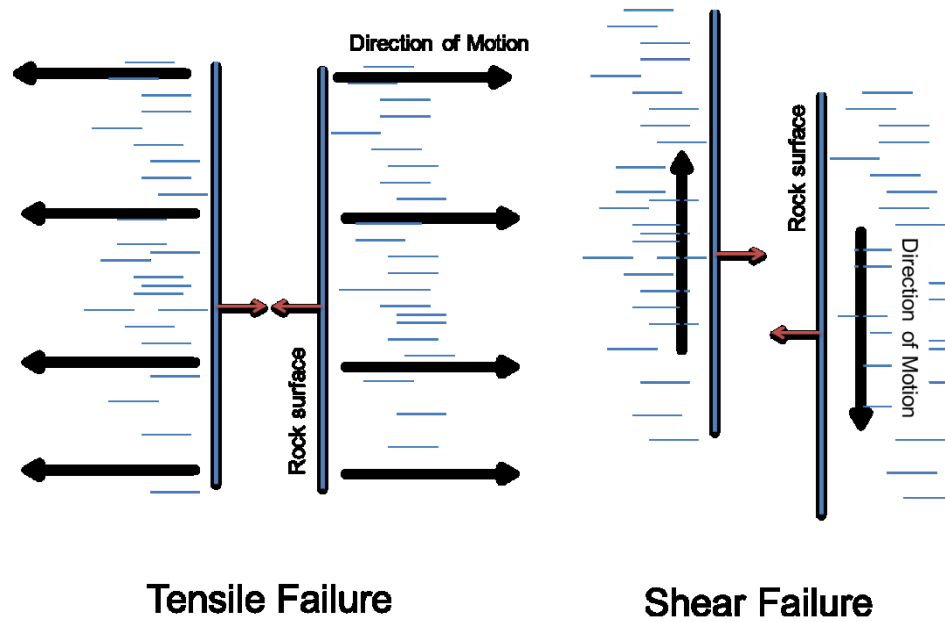


Figure 2: Modes of failure. Black arrows represent direction of motion and red arrows represent fracture surface direction.

To address issues associated with understanding and controlling fracture processes, laboratory and numerical studies on fracture response to material and stress conditions have applied focal mechanisms to establish relationships between micro and macro fracture structures. Seismic moment tensor and waveform polarity studies commonly are used to identify event focal mechanisms by examining the amplitude and relative direction of motion of the first arrival compression waves (Ohtsu and Ono, 1988; Manthei, et al. 2001; Shah and Labuz, 1995; Lei, et al. 1992; Zang, et al. 1998; and Stanchits, et al. 2006). Lei, et al (1992) examined sample fracture under triaxial compressive stress conditions and described the dependence of source mechanisms on the degree of heterogeneity. Fine-grained materials displayed an increased ratio of tensile events compared to course-grained materials. The authors proposed that typical fracture processes and corresponding acoustic activity could be described by three stages – initial closing, clustering, and final nucleation. Based on tests using Westerly granite, Reches and Lockner (1994) proposed a fracture model in which intact rock experienced fracture propagation through large scale micro cracking in front of the fracture tip,

followed by fault nucleation and extension through shear. Additional studies using creep loading reinforced the fracture mechanics theory of the process zone in front of the fracture tip and showed that shear activity dominated within a damage zone to produce macro-scale faults (Lei, et al. 2000). These laboratory tests suggest that global failure in competent material results from significant new fracturing produced by the fracture tip and not from intrinsic micro flaws coalescing into macro fractures (Reches and Lockner, 1994; Lei, et al. 2000). Tensile fractures induced through bending were also found to contain a large percentage of shear micro cracking, indicating local micro cracking is not a direct reflection of final macro fracture deformation (Kao, et al. 2011). Hydraulic fracture experiments also display the importance of grain size, permeability, fluid viscosity, flow rates, and the presence of local preexisting fracture networks on growth and focal mechanisms during stimulation (Lockner and Byerlee, 1977; Majer and Doe, 1986; Matsunaga, et al. 1993; Ishida, et al. 2004). Tensile microcracks are commonly associated with fine grained materials, higher flow rates, and higher viscosity fluids, whereas shear failures are commonly associated with course grained material, slow fluid pressure build up and lower viscosity fluids.

Microseismic and acoustic emission studies provide engineers and earth scientists an opportunity to examine failure processes in ways that strongly complement traditional geomechanic monitoring techniques. Of these, analysis of focal mechanisms is one of the most effective methods to characterize material failure because of its ability to describe fault planes, displacement types, and fracture propagation stages. Focal mechanisms have been used for decades by geophysicists to identify and characterize tectonic failures, and they will continue to play an integral part in characterizing fracture development for engineered reservoir systems.

1.2. Background

Hydraulic stimulation has been used extensively for resource extraction in a wide range of industries, including geothermal and petroleum energy. The stimulation process can be used as a method for measuring in-situ stress magnitudes, rock tensile strength, or to enhance permeability and access to a reservoir (Niitsuma, et al.1987; Whittaker,et al.1992; Ishida 2001). Linear elastic fracture mechanics theory as applied to hydraulic fracture load scenarios shows that fracture will occur in a well when the internally applied fluid pressure becomes sufficient to overcome the field stresses and tensile strength of a well wall. The tangential stress relationship at the wall of a well is provided in equation 1.

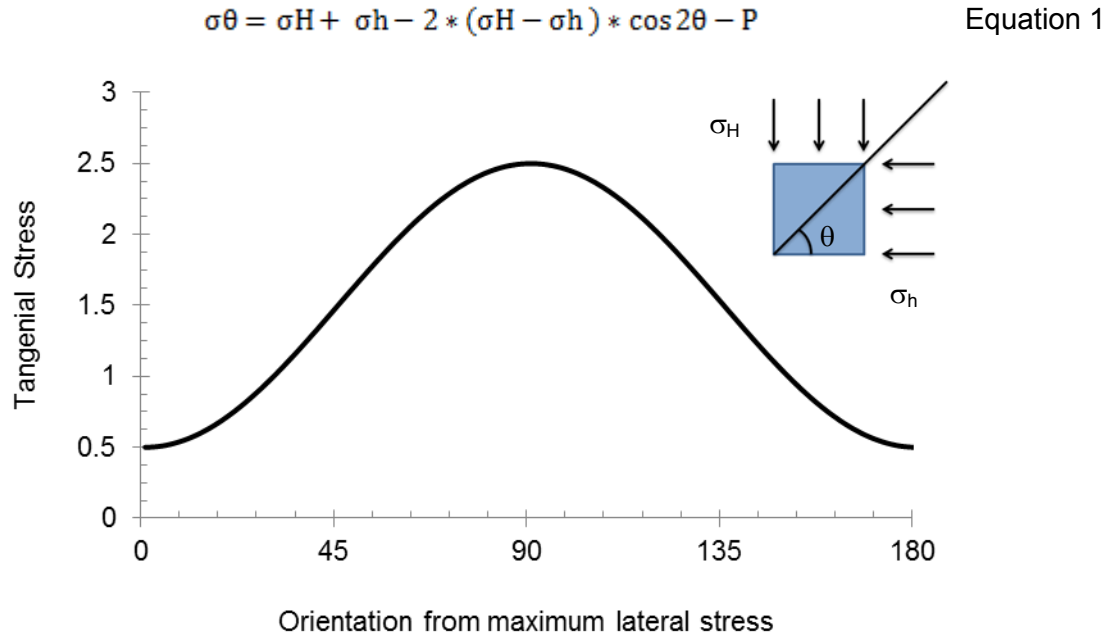


Figure 1: Tangential stress distribution as calculated using equation 1.

$$\sigma_H = 1; \sigma_h = 0.5; P = 0$$

Here σ_{θ} indicates tangential stress, σ_H and σ_h are the maximum and minimum lateral stresses, θ is the orientation with respect to maximum lateral stress direction, and P is the matrix pore

pressure. It can be seen that, in addition to the in-situ stress state, the tangential stress highly dependent on orientation with respect to σ_H and is minimized along the well parallel to the direction of maximum confinement and perpendicular to minimum confinement. Thus, the most likely location to initiate fracture is perpendicular to the acting direction of minimum confinement. Occasionally, linear elastic model estimates of pressure and orientation varies significantly from observed behaviors as a result of the complex nature of rock fracture processes and the significant variability in fluid viscosity, flow rates, stratigraphy, and in-situ stresses. A more holistic understanding of the fracture process is necessary to explain these differences, and to improve estimates of fracture parameters affecting breakdown requirements and stimulation effectiveness.

Many analytical models have been developed to predict the fracture growth behavior and resulting pressure response based on a variety of input parameters, including; simplified fracture geometry, fluid viscosity, and formation characteristics (Warpinski et al. 1994; Carter et al. 2000). Each model discussed makes width, length, and pressure predictions based on a particular set of assumptions unique to each model and results are sensitive to each. This makes prediction variable and subject to tweaking based on user experience. Fracture models created using numerical models have attempted to improve fracture assessment by incorporating failure modes, complex fracture geometries, and rock-fluid interaction (Al-Busaidi et al., 2005). Numerical models such as these benefit from detailed assessments of the fracturing mechanism at granular level which can be related to granular displacement magnitude.

Many researchers have approached the development of fractures induced by stimulation as the development of micro earthquake phenomena and applied many of the same techniques to its analysis. Acoustic emission technology aids in this assessment and has been used extensively in stimulation studies, both in the field and in laboratory. One of the benefits of

using an acoustic analysis method is the ability to confirm many of the results produced from analytical and numerical studies on rock fracture propagation. Fracture directions and areas of damage are identifiable from acoustic clouds produced from matrix failure under loading. Waveform amplitudes and frequency are dependent on the magnitude of surface displacement and size of fracture which can be directly compared to estimates computed from numerical displacement models (Majer and Doe 1986; Hazzard et al. 2000; Moriya et al. 2005). Studies can focus on a variety of statistical data regarding the spatial and temporal distribution of events (Becker et al 2010, Niitsuma et al. 1987), their magnitude relationship (Rao and Lakshmi 2005, Mogi 1962, Scholz 1968), and the displacement mechanism associated with failure (Ohtsu and Ono 1988; Shah and Labuz 1995; Zang et al. 1998; Dahm 1996). Using acoustic monitoring of these variables can provide additional insights regarding the process of propagation in a material. Theory concludes that tensile displacement modes are the main driving mechanism behind a hydraulically stimulated fracture growth. However, many observations show that shear events are often the dominant mechanism behind failure. Failure modes have been observed to fluctuate with changes to fluid viscosity, grain size, and the degree of heterogeneity of a specimen, which may explain some observed experimental differences in laboratory settings (Lei et al. 2002; Ishida 2001). The cause for the discrepancy is not fully understood but can be the result of signal loss in observation fields. It could also be a result of the changing stress field and fluid permeations into the matrix near the fracture. Majer and Doe (1986) showed that the actual fracture growth pattern resembled more of a propagation envelop with the hydraulic fracture surrounded by additional fractures. Tensile events were located along the main hydraulic fracture and shear events were closely related to but not associated with this plane. Sleaf, et al. (1995) also observed that shear type acoustic emission signals were associated with events located along the fracture plane but not directly associated with its creation. Therefore, it is reasonable to assume that fracture generation is the result of numerous mechanical fractures coalescing into a larger, general fracture. And, while a hydraulic fracture

itself may be generated by tensile failure, shear propagation modes will heavily influence its growth into the matrix.

Understanding the influence these parameters have on the fracture process is an essential part of more robust prediction models and stimulation evaluations. In order to reliably benefit from stimulation programs in complex rock strata it is important to know what methods produce optimal fracture propagations and to design treatments accordingly. Acoustic emission studies provide much of this information through source location, damage characterization, and descriptions of the mechanisms driving failure through the analysis of event waveforms magnitudes and characteristics. Additional research into the full implications of these impacts is necessary to advance the understanding of micromechanical failure process.

1.3. *Motivations*

The purpose of this study is to explore reservoir characteristics and formation response to stimulation treatment of simulated geothermal reservoirs. Acoustic monitoring technology is used to examine fracture geometry created during stimulation so production wells can connect with the activated fracture network. Characterization of the wells is required to explore the effectiveness of stimulation treatments and to provide information for determining the need to update treatment plans. Lastly, describing the fracture process and understanding the impact that fluid viscosity, confining stress, and grain size have on the formation process is important when designing treatments. This work examines these impacts by studying stimulation treatments in 3 granite samples.

1.4. *Objectives*

The main objective of this work is to hydraulically stimulate EGS samples and to use acoustic monitoring technology to identify fracture geometry and location for simulated geothermal production well placement. An additional objective is to characterize the fracture

process by monitoring changes to waveform characteristics during propagation. Waveforms are dependent on the type and magnitude of surface displacement during fracture. Therefore, analysis of these waveforms and their changes provides important descriptive information regarding the magnitude and distribution of fracture networks resulting from stimulation.

2. METHODOLOGY

2.1. *Test equipment*

Laboratory equipment used to complete testing for this project included a custom designed true triaxial cell, two syringe pumps, and LabVIEW-based data acquisition and command programs. The triaxial cell contains three active steel platens and two passive cement platens to confine the sample. Each active steel platen has machined ports and guides to hold the acoustic sensors against the sample face and to guide the cables out of the cell. The two cement platens are poured once the sample has been seated. Pressure from the flat jacks inside the cell is used to press the sample into the cement so that the cement will conform to any potential imperfections on the surface. This improves stress uniformity applied at the boundaries. Confining pressures up to 13 MPa are applied to each axis and controlled through the use of three hydraulic pumps. The cell was designed to hold samples sized 30x30x30 cm³. Heating elements located on the sides and bottom of the triaxial cell were capable of producing temperatures up to 180 °C. Specimen temperature was maintained using insulating bricks. The dual syringe pumps were capable of pressures up to 70 MPa and flows of $1 \times 10^{-5} - 6 \times 10^1$ mL/min. Custom LabVIEW controls maintained either constant pressure or constant flow states. A total of twenty strain gauges and sixteen thermal couples could be used during a test. Measurements of strain, temperature, pressure, mass, and flow data samples using the LabVIEW programs acquired data at a rate of 1 sample per second. Injection and production wells were created using a percussive drill. Forming wells percussively is expected to create additional similarities between field and laboratory environments because of the damage created in the well and nearby material. A drilling frame with angles of 0, 15, and 30 degrees

from the vertical axis allowed injection and production wells to be drilled while the sample was confined at pressure and temperature inside the cell.

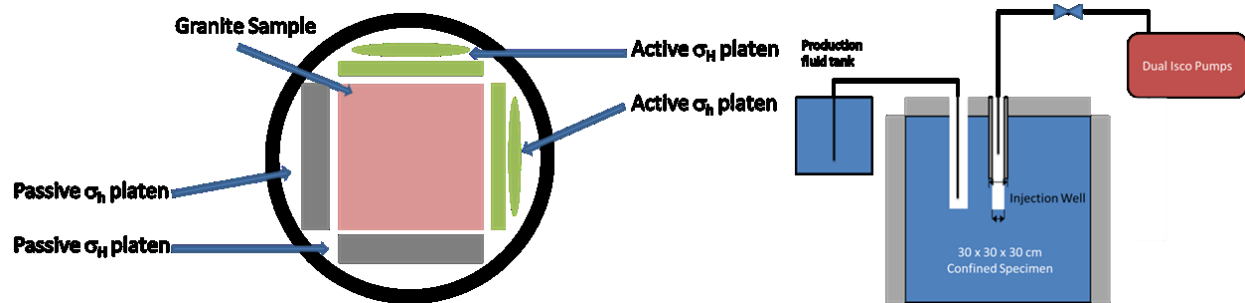


Figure 3: Simple diagram of the triaxial cell and its fundamental components.

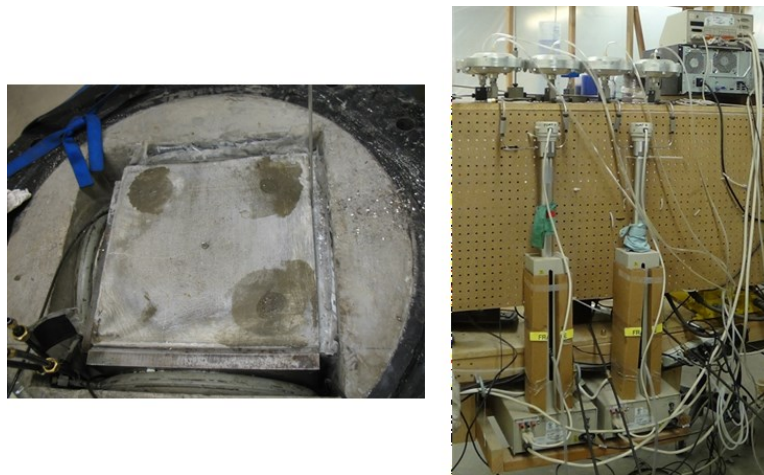


Figure 4: Image of a loaded sample inside the triaxial cell (left) and dual pump injection system (right).

Injection wells contained cased and uncased intervals. Threaded steel pipe lined the cased interval and was sealed using epoxy. No perforations were added to the steel casing and the uncased interval below the pipe was used for as the stimulation interval. Additional detail on the design and capability of laboratory equipment and software may be found in Frash (2012).

2.1.1. Injection Fluid

Several fluids were used for stimulation testing and included a slow cure commercial epoxy, oil, and water. The epoxy fluid had a working time of 60 minutes and was allowed to cure within the stimulated fracture. Viscosity for the epoxy was approximately 80×10^3 cP. The stimulation oil was commercially available Valvoline SAE 80W-90 gear oil with an estimated viscosity of 71.5 cP at a temperature of 50 °C using ASTM D341-09. Water used during treatment was local public tap.

2.1.2. AEwin and software

The equipment used to record laboratory acoustic emissions include six piezoelectric sensors, six 2/4/6 preamplifiers, and AEwin software supported on a Physical Acoustics Corporation (PAC) PCI-2 platform. Wideband WS Alpha piezoelectric sensors were selected based on the operational frequency bandpass and temperature range required to support EGS stimulation experimentation (Table 1). Waveforms were amplified with either 40 or 60 decibel preamplifier gain prior to being recorded by the system and saved to disk. Each preamplifier was capable of performing an Auto Sensor Test (AST) that generates an electrical pulse and deforms the piezoelectric crystal and generates a waveform detectable to other active sensors in the array. Auto sensor tests could be used to test for communication issues with a channel, confirm distances between sensors, or to measure wave velocity through sampled travel times from source to time of trigger. Three dual channel PCI cards capable of cumulative sampling rates up to 40 mega samples per second (40 MSPS) were connected to each WS Alpha sensor through the preamplifiers. Unconfined samples were monitored using six sensors fixed to the sample face with silicone caulk. For confined samples, preparation of the triaxial cell required a couplant capable of maintaining a sensor-to-sample connection with low risk of debonding in cases of slight shifting. This connection was provided using a coupling material and a housing system in order to hold the sensors against material surfaces for a continuous connection to the sample. Silicone vacuum grease was selected for confined experiments based on its listing in

the PAC manual as an appropriate coupling material. The steel platens used in the triaxial cell were machined to fit the sensor and cable, thus providing an abutment for the sensor. Foam backings and sleeves were used to maintain face pressure while dampening acoustic signals that arrived from the sides or back of the sensor (Figure 5). Additional sensor and preamplifier specifications are provided in the appendix and may be found in the reference PAC (2007).

Table 1: Acoustic sensor characteristics

Sensor dimensions (mm)	19 dia x 21.4 h
Temperature range (°C)	-65 – 175
Operating Frequency (kHz)	100-900
Resonance (kHz)	125 V/(m/s), 650 V/□bar
Peak Sensitivity (dB)	55 V/(m/s), -62 V/□bar
40 dB gain preamp bandwidth (kHz)	10 – 900
60 dB gain preamp bandwidth (kHz)	10 – 2000



Figure 5: Platen, acoustic sensor with preamplifier, foam sleeve and backing

Acoustic data collected during monitoring of samples are composed fundamentally of hit data. Events are located using a minimum of four triggered sensors and a regression type minimization of travel time residuals between a modeled source and measured data. Error for each event is quantified in a quality coefficient ranging between 0 and 1. The coefficients are scaled between 1 and 10 when plotted in MATLAB, corresponding to minimum and maximum values accordingly. Additional data can be collected for a test by further analyzing hit waveforms based on a set of components describing the structure of a hit. Hit data consist of a waveform collected at a sensor with signal crossing a minimum amplitude threshold level. Additional samples are recorded preceding the first threshold crossing and some duration of time after the last crossing. This wave structure can be described using the basic components provided in the ideal wave represented in Figure 6. The AE Threshold level is the minimum signal amplitude needed to trigger a wave record at a sensor with this time described as the time of hit. Wave amplitude is the maximum signal magnitude to occur between the Time of Test and the last threshold crossing or AE Duration. Rise time is the time required for a signal to reach its maximum amplitude after the Time of Test. Hit Definition Time is the maximum length of time a signal may be recorded, even if its amplitudes still cross the threshold (MISTRAS, 2011). Hit Duration is the amount of time signal amplitude crosses the threshold. Once amplitude remains below threshold waveform recording is stopped. Records were taken at a rate of 1 MSPS and were 1024 sample long for files 0.001 second in length. Two hundred and fifty six elements of background before the arrival of the first threshold crossing are reserved in each file.

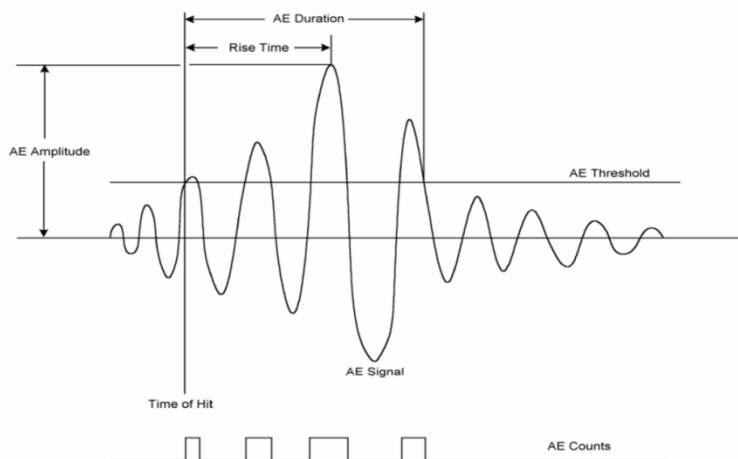


Figure 6: Idealized waveform for component description (PAC 2007)

2.1.3. Test Materials

Colorado Red Rose granite specimens obtained from a quarry near Lyons, CO and synthetic rock material created from high strength concrete were used to create enhanced fracture paths for EGS study. Granite was chosen for its commonality as crystalline bedrock in HDR EGS fields and its relative homogeneous nature. Many of the samples contained bands of similar material that were lighter in color and contained crystals that varied in size from the rest of the material. The surface of the samples did not contain noticeable fractures. The Young's modulus, Poisson's ratio, and unconfined compressive strength for this batch of samples were 57 GPa, 0.32, and 152 MPa, respectively. Additional properties are listed in Table 2.



Figure 7: Sample G01-93 with sensors attached

Table 2: Typical Colorado Red Rose granite characteristics

E [GPa]	57
UCS [MPa]	152
BTS [MPa]	7.3
ρ_{dry} (kg/m³)	2650
V_s (mm/sec)	2.62×10^6
V_p (mm/sec)	4.45×10^6

3. TEST RESULTS AND DATA

3.1. Sample G01-91

Sample G01-91 was tested under isotropic atmospheric conditions using an epoxy injection fluid. The goal of this test was to stimulate a complex fracture network by eliminating the preferential fracture direction created from differential stress environments. Epoxy was selected as the stimulation fluid so that any dilated fracture apertures would remain at least partially open and be filled in order to allow observations on the extent of fluid propagation into the fractures. Using linear elastic fracture mechanics theory, the breakdown pressure for this sample was estimated to be approximately 7.3 MPa based on the typical tensile strength exhibited by core samples using Brazilian tensile tests. Fracture initiation occurs when fluid pressure within the injection well reaches a critical level P_{frac} , presented below in Equation 2. Here σ_h is the minimum horizontal confining stress, σ_H is the maximum horizontal confining stress, P_p is the rock mass pore pressure, and T is the rock mass tensile strength. In this test breakdown occurred at an injection well pressure of approximately 51 MPa. The reason for the difference between observed and predicted breakdown pressures is not immediately known.

$$P_{frac} = 3\sigma_h - \sigma_H - P_p + T \quad \text{Equation 2}$$

$$P_{frac} = T \quad \text{Equation 3}$$

Twenty strain gauges were attached to four vertical faces of sample G01-91 using two layouts as illustrated in Figure 8. Because the sample was unconfined, silicone caulk was used to fix

the sensors to the sample faces. Gauge locations were optimized to increase the coverage of areas likely to interact with a propagating fracture. Fractures did not have a preferential propagation direction that could be used to guide gauge placement because of the isotropic stress state. In addition, sample G01-91 contained a band of material containing crystal distributions and sizes that are different from the main rock matrix. This band passes diagonally across the entire block.

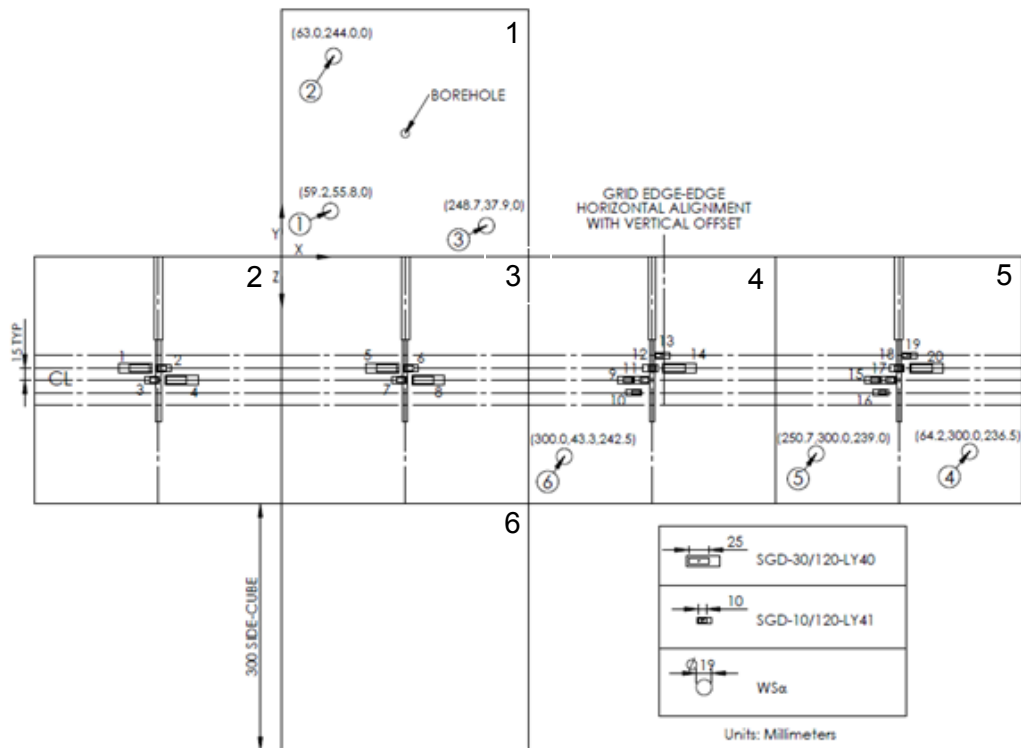


Figure 8: Location of strain gauges and acoustic sensors on Sample G01-91.

The injection well for the test was drilled vertically into this coarse band to minimize its influence while the fracture propagated. The injection interval was a 10 mm diameter vertical well drilled vertically to a depth of 150 mm into the sample. Steel casing was placed to a depth of 100 mm. The last 50 mm were uncased to allow for stimulation. Treatment occurred by filling the injection well with a mixed epoxy fluid and using high pressure water to force the epoxy into the rock matrix at a rate of 0.05 mL/min. Measurements of pressure, ambient air temperature, and

acoustic emission were collected during the preparation, stimulation, and curing stages of the test. Estimates of acoustic wave velocity from AST and PLB tests were 4.7×10^6 mm/s and 4.6×10^6 mm/s, respectively. Testing was completed using a threshold of 25 dB and sampling rate of 1 MSPS. Frequency bandpass was 1 – 400 kHz.

3.1.1. Pressure and Acoustics

Acoustics are defined as all collected waveform and localized event data over the course of stimulation. Histograms of hits and figures of event locations are presented with respect to time and referenced against other data (i.e. pressure, strain, etc.) for behavior analysis. Figure 9 shows the pressure and hit count over time as recorded during the stimulation test. Pressure rise time for the main breakdown event was approximately 1800 seconds, from the start of constant flow at about 3500 seconds to breakdown at about 5300 seconds into treatment. Figure 10 and Figure 11 illustrate changes in acoustic emission rate, amplitude spread, and pressure during the main fracture interval between 5000 and 5600 seconds into stimulation. This window begins with activity leading up to the main breakdown event and ends with activity occurring after a secondary breakdown stage. During the injection process, acoustic emissions produced distinct stages of output that varied over time and corresponded with substantial changes in pressure. The first stage of acoustic emission activity begins at low levels but increases noticeably after 5200 seconds. Maximum activity for stage 1 occurs immediately after 5300 seconds and corresponds to the first decline in well pressure during treatment. The b-values for hits collected during this stage are generally high but fluctuate in magnitude. A note of interest is the lag experienced between acoustic activity levels and the change in pressure during this stage. Activity in stage 1 is interpreted to correspond to the activation of micro-fractures that exist naturally or are formed at grain boundaries due to stress concentrations resulting from increasing stress in the well. These micro-fractures may then coalesce into macro-fractures, which grow into the sample and create additional micro-fractures ahead of the

advancing fracture tip. During this process fracture deformations increase and is reflected by the amplitude spread, or changes to number of large amplitudes relative to small amplitudes. Wave amplitude is known to be proportional to fracture surface displacement and the number of large events relative to small events should increase once significant coalescence begins and larger displacement occurs. One way to observe this change is to calculate the seismic b-value within a specified window or using a minimum number of hits to measure relative changes in this value during the fracture process. An increase in activity suggests an increase in damage from loading and an increase in wave amplitudes suggest an increase in damage intensity. Stage 1 therefore, corresponds to increasing levels of damage and damage intensity.

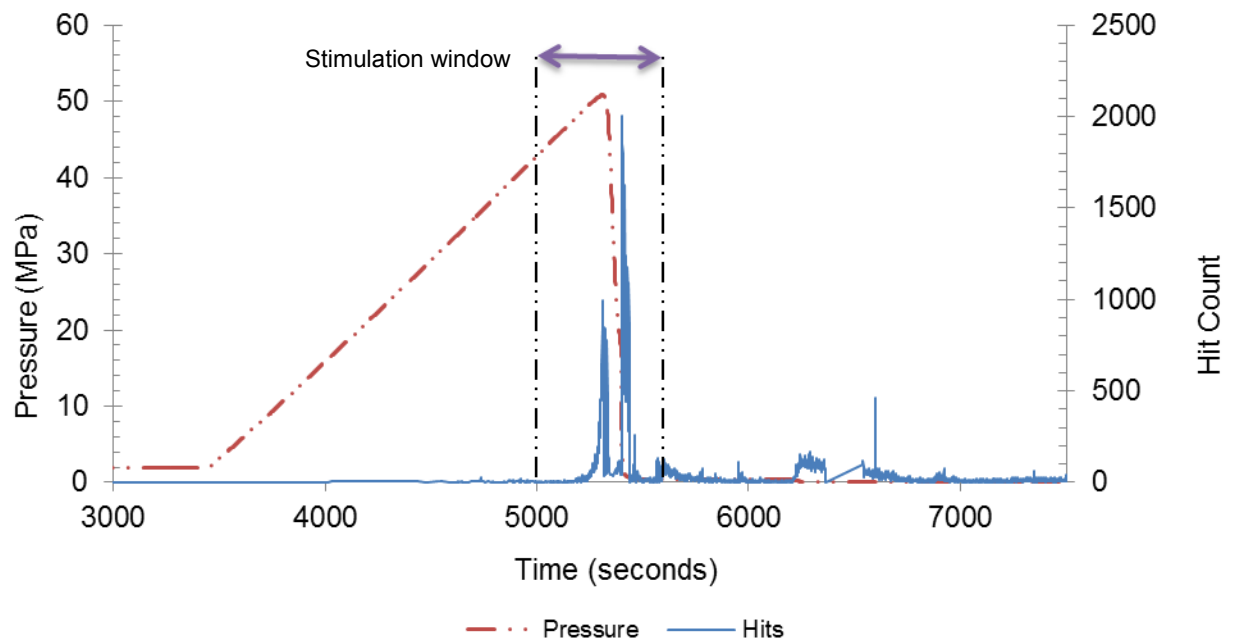


Figure 9: Pressure and hit activity in one second bins for the duration of stimulation.

A second stage of fracture activity lies between approximately 5320 to 5400 seconds (Figure 10) and contains fewer hits than the first stage. However, the amplitudes associated with this part of the fracture process are much higher overall. Furthermore, this stage of the fracture contains an increasing rate of activity until about 5400 seconds into the test. The rate of pressure loss during this stage decreases as well, corresponding to the changes in acoustics.

Stage 3 occurs after 5400 seconds and contains another large increase in acoustic activity. This second peak is preceded by an additional sharp pressure drop. Pressure levels at the time of high activity are low, however, and the amplitudes during this time interval decrease (Figure 11). Additional commentary regarding stages 2 and 3 are provided below in the section titled *Strain and Acoustics*.

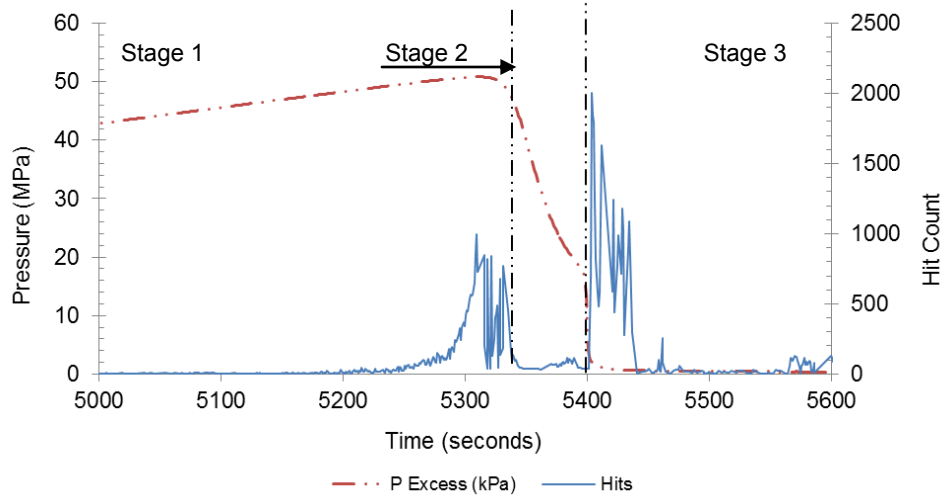


Figure 10: Window of the stimulation time interval at 5000-5600 seconds (highlighted in Figure 9). Several stages of fracture can be identified through changes to pressure and hit counts.

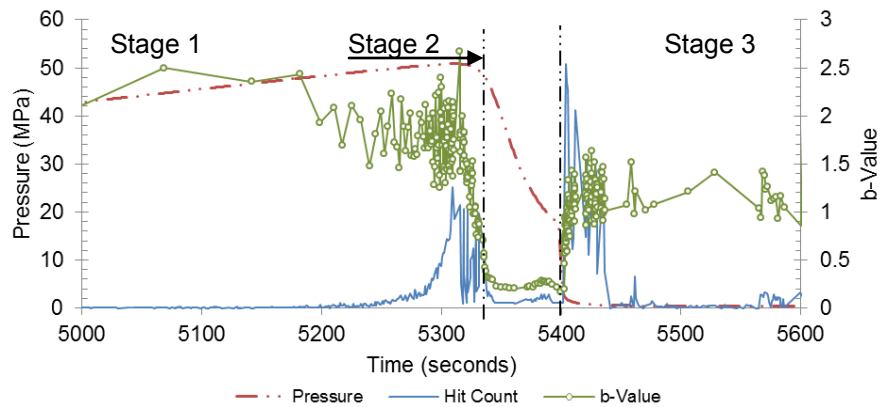


Figure 11: Pressure and amplitude spread for sample G01-91 at 5000-5600 seconds (highlighted in Figure 9). Hit counts are plotted relative to pressure, with max hit rate equivalent to max pressure.

3.1.2. Pressure and Strain

Measurements of strain taken during the test displayed distinct changes that correspond to changes in pressure (Figure 12). Each gauge displayed is from one vertical face of the sample. Gauges 1 and 13 were located on opposite faces parallel to the direction of fracture propagation, whereas gauges 6 and 17 were located on opposite faces normal to the direction of fracture propagation. Negative measurements of strain represent tensile displacements and positive values represent compressive displacements. All gauges display tensile displacement during most of the fracture process, although gauges 6 and 17 have distinct reversals near the end. Significant dilation at breakdown indicates fracture propagation into the sample. Gauges begin measuring significant tensile readings at approximately 5320 seconds into the test which corresponds to rapid declines of injection pressure. The rate of pressure reduction declines between about 5370 and 5400 seconds, suggesting that increasing energy is required to maintain fracture propagation into the sample. Strains along the two faces parallel to the fracture also reach their maximum level. After approximately 5400 seconds, the second pressure drop is experienced and gauge 6 fails while gauge 17 measures compressive strains. This process indicates that the second pressure drop is associated with fracture propagation to the sample surface and interception with the gauge. Once the fracture reached the surface, opening motions forced the back to act as a hinge and caused compressive force redistributions. Based on the visual location of fractures within the sample, gauges 6 and 8 were both intercepted by the fracture which would have caused them to fail. Gauge 17 was located on the opposite face and no fracture was observed along this surface. These observations suggest this was the most likely process.

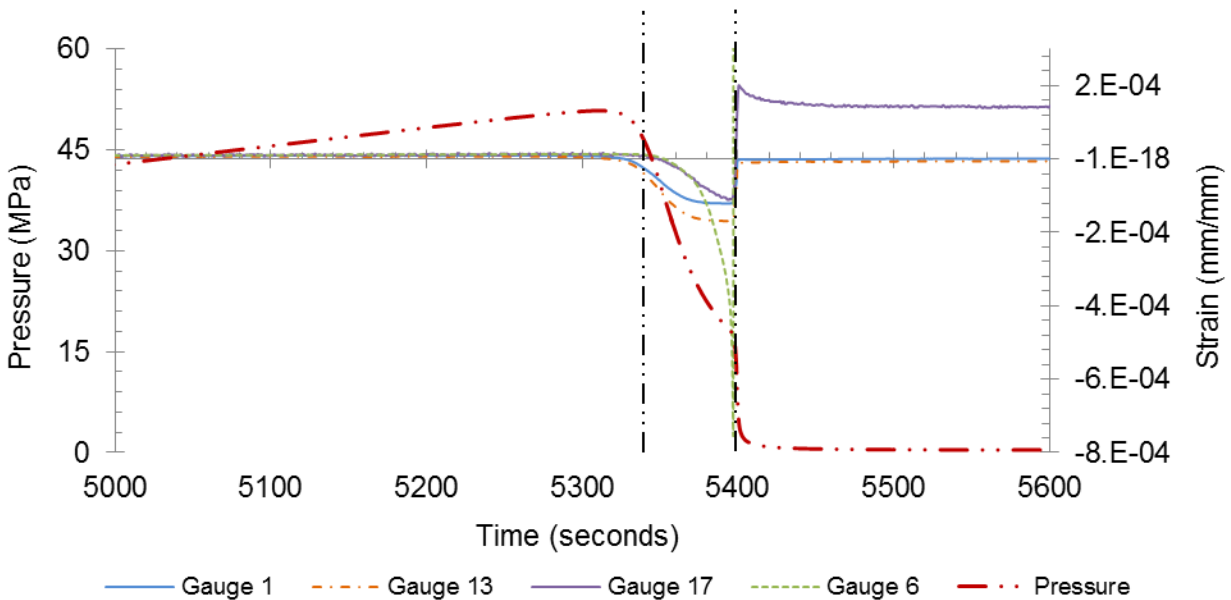


Figure 12: Pressure and strain readings from 5000 to 5600 seconds for sample G01-91. Note the distinct variation in strain for the four different gauges.

3.1.3. *Strain and Acoustics*

Comparison of changes in acoustic emissions and strain during fracturing highlights the relationship between these two methods of measurement (Figure 13). On this graph pressure is scaled as a percentage of the maximum hit rate for reference. Stage 1 of the acoustic activity occurs mostly without significant changes to strain measurement. However, starting at approximately 5300 seconds, and continue thereafter, sustained acoustic activity displacement begins to increase. Once fluid begins to leave the well and fracture propagation likely begins in the sample, strain increases at a higher rate. During the second stage hit count is reduced but wave amplitudes are greater than in the first stage of the test. The observed pattern suggests that fracture surface displacement has increased relative to early fracture stages. This relationship is further supported by the strain readings. Acoustic activity again increases during propagation between 5300-5400 seconds and corresponds closely with the decreasing rate of pressure loss. The increase in acoustic activity and pressure required to maintain flow indicates that fracture propagation was unstable immediately after breakdown, but began to stabilize as

propagation continued and fracture size increased. At the point of final pressure drop, the acoustic and strain data show considerable change. The gauge failure and compression readings correspond to the last increase in acoustic output, but the event magnitudes are comparatively low. Because no fracture was detected at the opposite end of the sample, it is reasonable to surmise that the fracture propagated in both directions in a two wing format until one of the fractures reached a critical length in the sample. At this time, the sample was unable to hold the growing fracture and it reached the surface by unstable extension. The newly formed fracture wedged open the sample and produced large compressive forces at the opposite end of the sample. As a result, many of the events produced were likely induced by the stress redistribution created by the structural alteration.

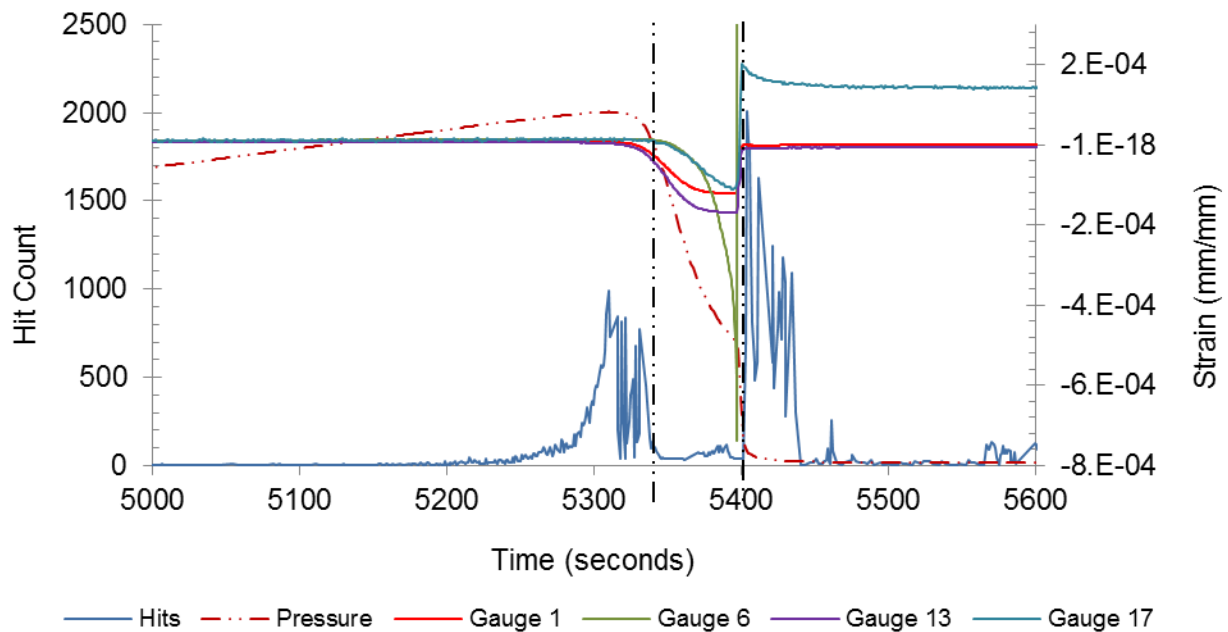


Figure 13: Acoustic hit count and strain between 5000 and 5600 seconds graphed together for sample G01-91. Pressure scaled relative to hit counts

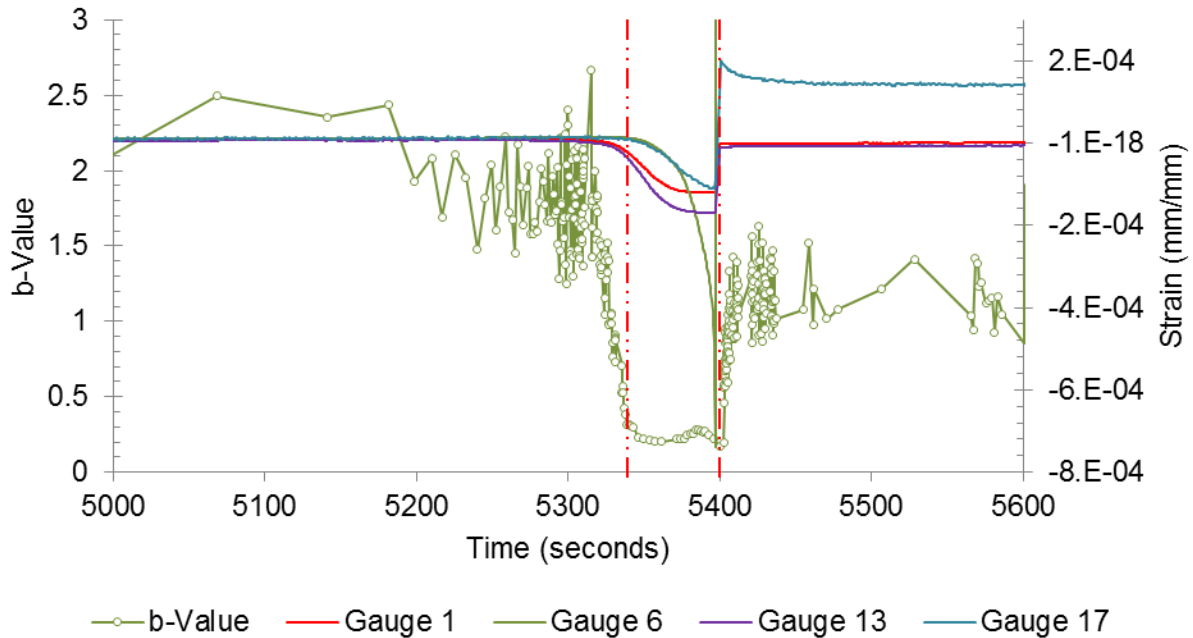


Figure 14: Strain gauges and b-value from 5000 to 5600 seconds graphed together for sample G01-91. Strain gauge 6 failed where the line goes vertical.

3.1.4. Geometry

The fracture grew in a bi-wing formation despite the opportunity for enhanced complexity provided by the isotropic stress condition. Visual observation verified that the fracture did extend to the sample surface and had crossed directly through stain gauges 6 and 8, resulting in failed readings near the end of the test. The second wing did not reach the vertical surface on the opposite face but did have fracture observable from the top of the sample. Event locations were used to predict the most likely area of fracture based on relative density near a theoretical fracture plane rotated through the sample using the positive x-axis for the reference plane. Density increased to a maximum at approximately 270 degrees rotation from the reference and corresponds to growth in the negative y-axis (Figure 15). However, the density results also contain additional lesser peaks which may indicate multiple fracture planes in other areas of the sample.

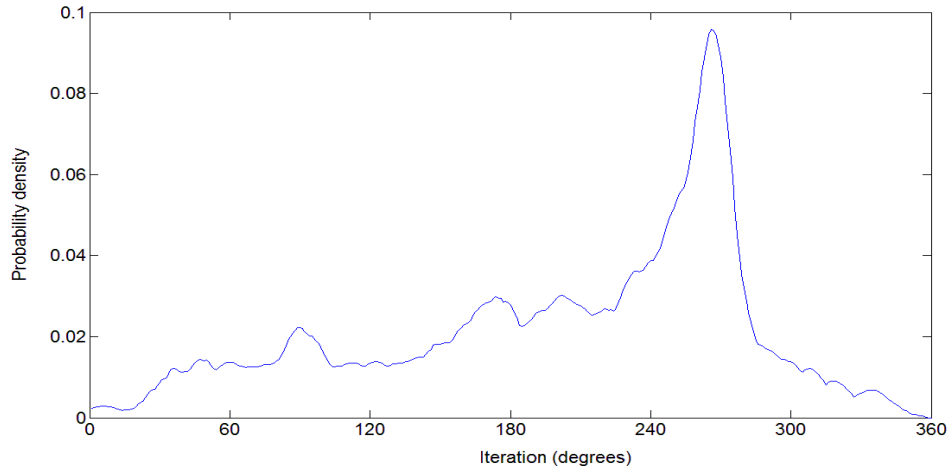


Figure 15: Estimate of fracture location from all events in sample G01-91. Events locations are relative to a theoretical plane rotated through the positive x-axis.

When viewing events in the context of the previously characterized changes in acoustic output, the location of such events appears to change over time. These changes likely correspond to variations in the fracture process and result in different areas of damage. Located events created in the initial loading period prior to breakdown are presented in Figure 16 and occurred between 4000 and 5300 seconds with respect to hit rate. The size for each point on the plot is proportional to amplitude with increasing size representing increasing amplitude. The color is dependent on the positional confidence of events as indicated through a correlation coefficient. Events plotted with cooler colors have lower positional confidence, starting with a minimum correlation coefficient of 1. Events plotted with warmer colors have higher positional confidence and can reach a maximum correlation coefficient of 10. The majority of stage 1 events are located near the injection well, but lower amplitude events also highlight the possibility of a secondary plane activated during stimulation. Events lying on this plane correspond closely to the coarser crystalline zone in which the injection well was placed, suggesting activation at high stress areas present from the formation of this zone or as a result of increased stress concentration at the boundaries of the larger crystals. The second stage of fracture produces a similar outlay of events as stage one and can be represented by Figure 16

as well. Stage 3 of the fracture process occurs after the last major drop in pressure between 5400 and 5600 seconds. These events are concentrated along the fracture plane and spread nearly from face to face of the sample in the y and z axes. Events in this location may indicate activity associated with stress redistribution after the fracture reached the surface and altered the structure of the sample (Figure 18).

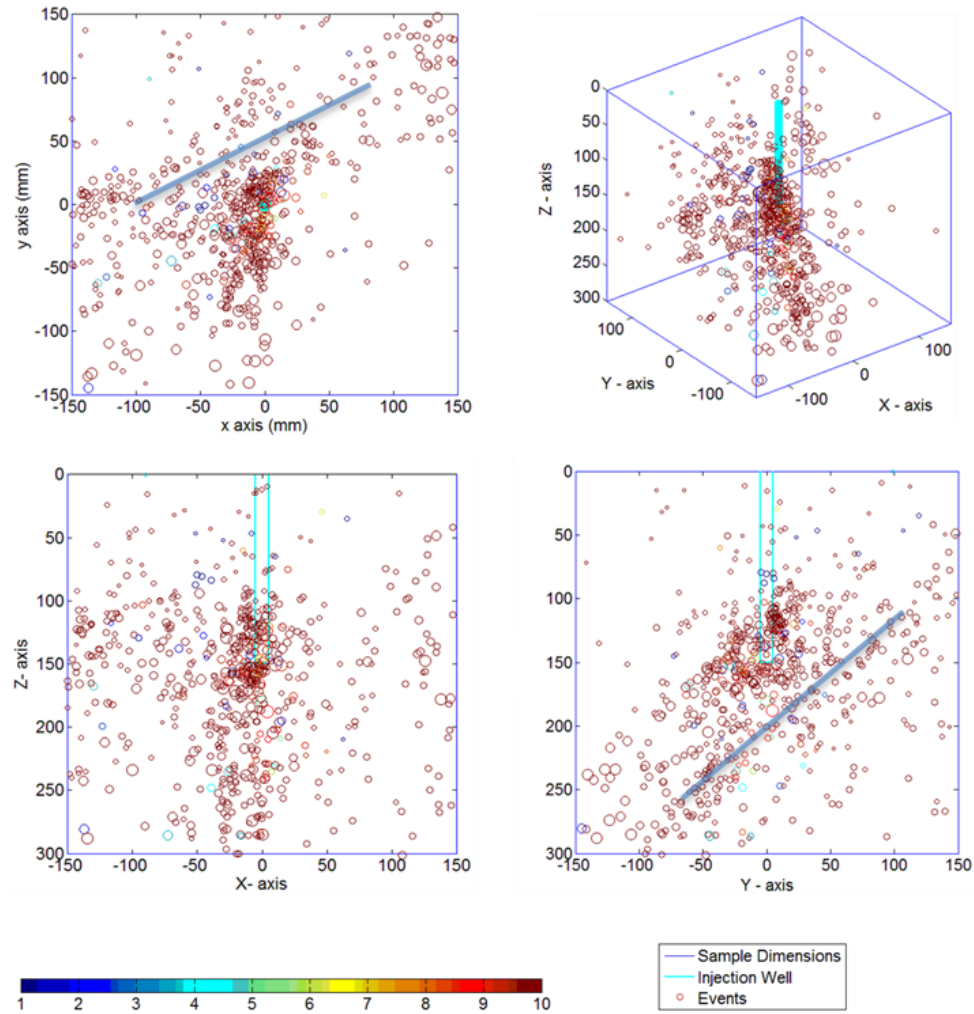


Figure 16: Stage 1 events

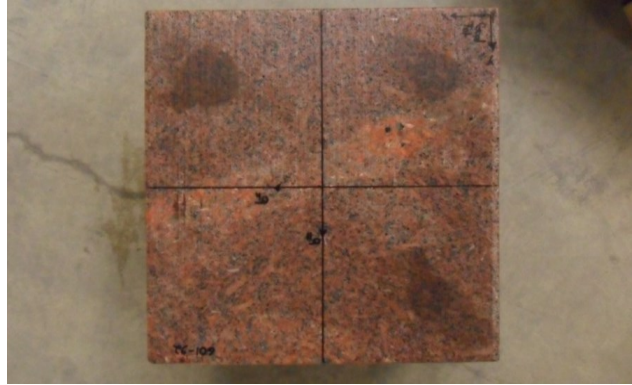


Figure 17: Top view of sample G01-91. Note the band of coarser crystalline material running diagonally across the middle of the sample from left to right.

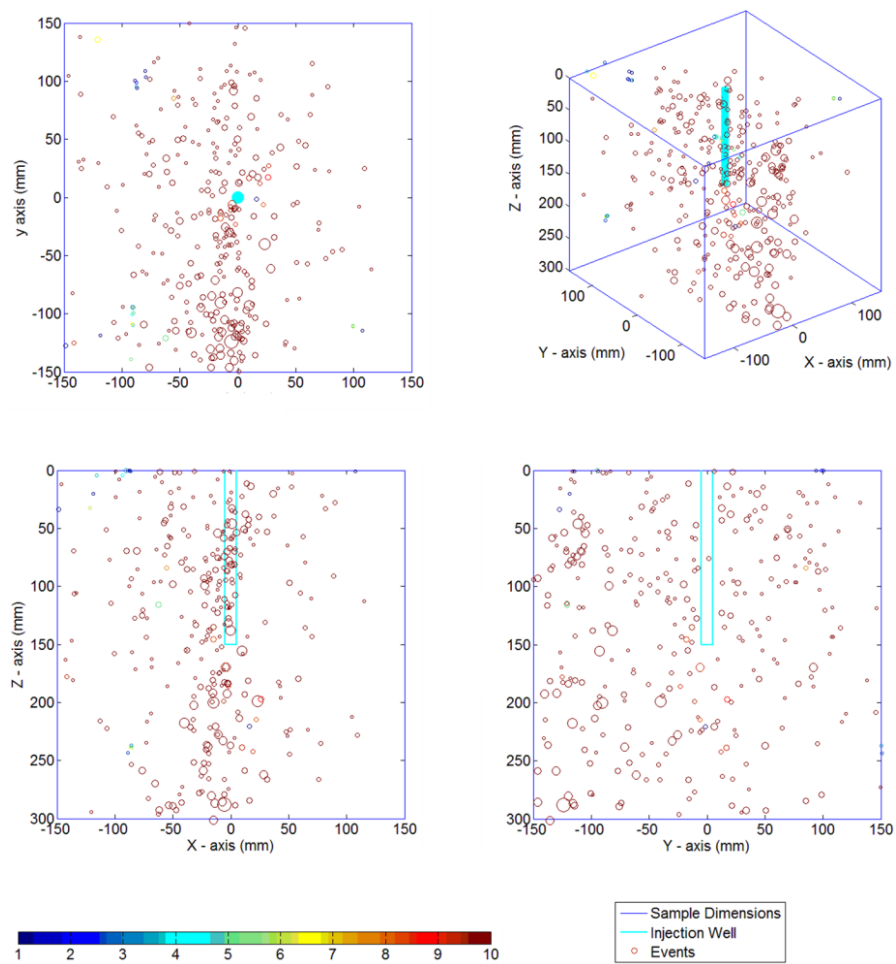


Figure 18: Stage 3 events

Sample G01-91 was an unconfined granite specimen stimulated hydraulically using epoxy as the injection fluid. Acoustic monitoring was used in conjunction with strain and pressure to observe and analyze the fracture propagation. Hit counts and amplitude provided important information regarding the relative amount and severity of damage induced from loading. Strain and pressure data also described behavior and highlighted different stages of fracture propagation that were complementary to acoustic records. Event locations and fracture geometry was well represented by acoustic emissions and enable spatial descriptions of areas damaged by loading. In this example, the hydraulic fracture location is well identified by the number and magnitude of events surrounding it. In addition, an area of significant variability was evident in events located near a secondary material band at the center of the sample. Unlike the events associated with breakdown, no macro-scale fractures propagated in this direction.

3.2. Sample G01-92

G01-92 was a triaxially confined sample given isotropic lateral confining stress and maximum confining stress in the vertical direction. The stimulation fluid was local tap water and contained no proppant. The main goal of this test was to produce a complex vertical fracture network with treatment. It was believed the best opportunity to reach this goal was to use isotropic lateral stresses and low viscosity fluid during stimulation. Treatment included a series of constant flow stages to induce fracture through stimulation. Multiple flows trials were required because uncharacteristically high permeability created pressure-flow equilibrium and breakdown was not achieved with the conventional flow rate. Stimulation began with a previously applied flow rate of 0.05 mL/min and doubled with each repeated trial with the exception of trial three. Breakdown occurred at a flow rate of 1.6 mL/min or 32 times the flow expected from previous tests. A 10 mm diameter injection well was placed at the center of the sample ($x = 150$ mm, $y = 150$ mm) and drilled to a depth of 100 mm while the sample was under full confinement. This interval was then cased and sealed using steel tubing and an additional 50 mm was drilled

beneath. Interval 2 was left uncased for stimulation and a total well depth of 150 mm was achieved. Confining stress in the lateral directions was 8 MPa with maximum confinement in the vertical direction reaching 13 MPa. Isotropic lateral confinement according to linear elastic fracture mechanics theory removes the field stress preferential fracture direction and provides opportunity for multiple fractures to propagate with breakdown. In addition, a low viscosity fluid such as water may also increase complexity because it will more readily leak into the rock matrix, lower effective stress due to increased pore pressure, and lower the material strength around the propagating hydraulic fracture. Estimated breakdown pressure from linear elastic fracture mechanics was approximately 23 MPa and was close to the observed 28 MPa. In addition, the breakdown pressure and first re-stimulation pressure were approximately 6.2 MPa different, very near the expected tensile strength for these samples and in accordance with linear elastic theory.

The sample was prepared at a local privately owned stone cutting facility to polish the faces and improve tolerance within the cell. However, some fluctuations along the face were not removed and it was decided to fill any possible gaps that lie between the steel platen and face to improve stress distributions at the boundaries. Twenty strain gauges were placed on the four vertical faces of the sample prior to placing the concrete. Gauges were arranged in two patterns in order to optimize their effectiveness during the test (Figure 20). Since no fracture direction was predicted prior to stimulation the gauges were laid to provide wide coverage while maintaining some degree of resolution. After the gauges were prepared a thin layer of cement was cured between the active platen their respected face to improve contact. The thickness was greater than space available for acoustic sensors to directly contact the sample face and a wave guide was necessary to maintain contact. Rather than used the cement mixture, granite disks were cut from additional cores of Colorado Red Rose granite to fill these gaps to minimize changes in acoustic properties at the sensors. Measurement of velocity and attenuation were

taken before and after the sample was placed inside the confining cell using auto sensor and pencil lead break tests (Table 3). Frequency bandpass for this test was 1 – 400 kHz with a sampling rate of 1 MSPS. The recording threshold was 25 dB.

Table 3: List of sample acoustic properties

Test Stage	AST Velocity (mm/sec)	PLB Velocity (mm/sec)	Attenuation (dB/m)	PDT (μs)	HDT (μs)	HLT (μs)
Out of Cell	3.6×10^6	4.7×10^6	88	50	50	2
In Cell	3.4×10^6	N/A	74	50	150	2

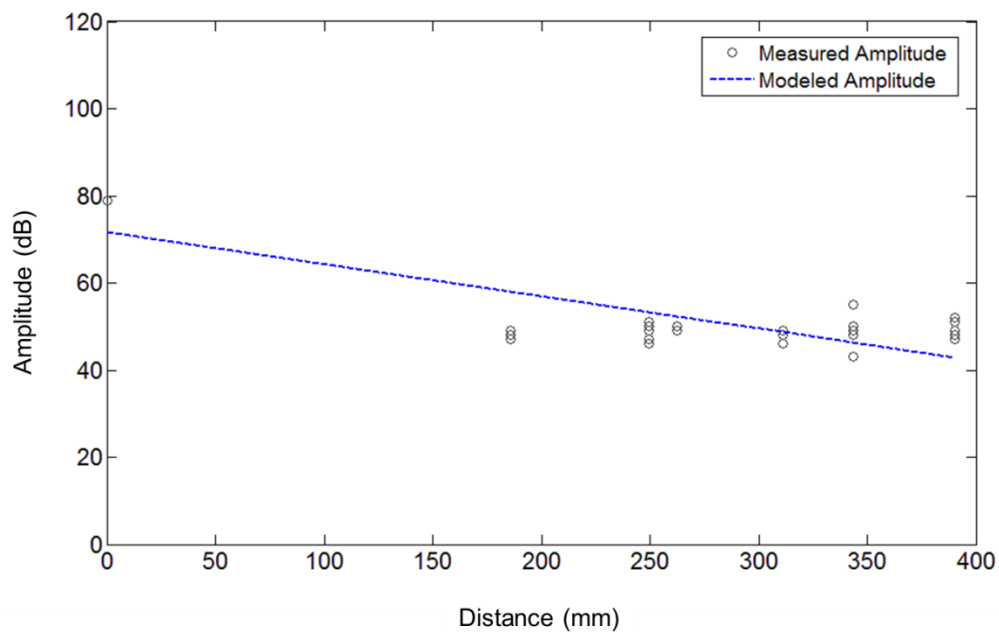


Figure 19: G01-92 loaded sample amplitude measurements

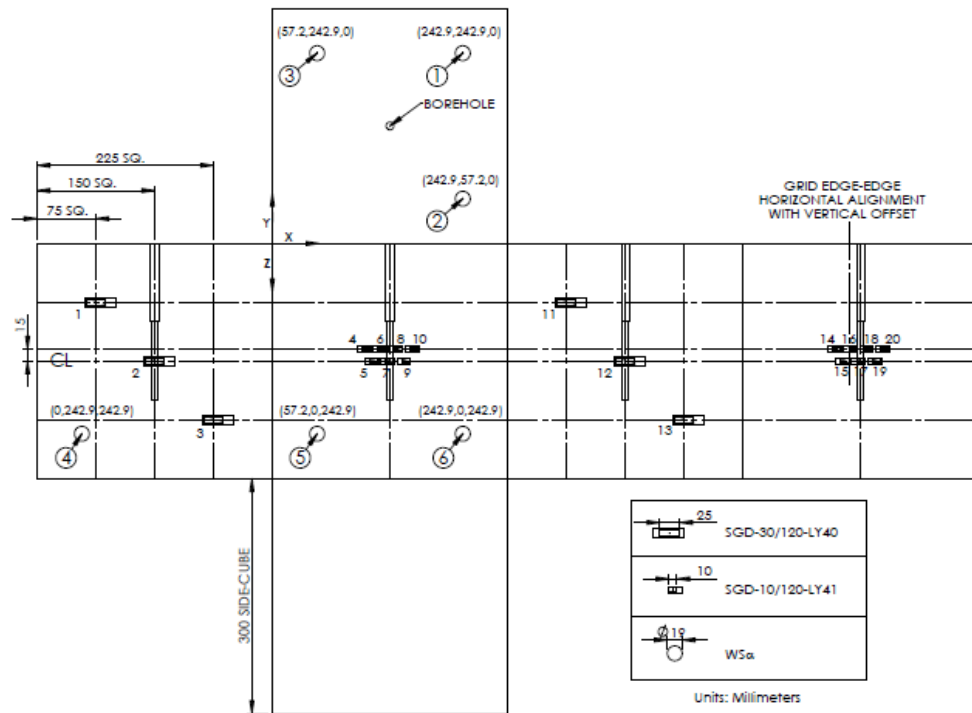


Figure 20: G01-92 strain gauge layout

3.2.1. High Initial Permeability

A 2 MPa pressure cycle was conducted prior to stimulation in order to provide a basis for assessing the effectiveness of the stimulation treatment. During this first interval, the fluid volume passed was high compared to expectations for the granite specimen. Typical experiments used stimulations injection flows at 0.05 mL/min to induce breakdown. From Figure 21 a constant pressure of 2 MPa shows an average flow rate nearly 0.018 mL/min prior to stimulation and is approximately 36 percent of the expected flow at stimulation. Likely causes for initially high fluid flows were leaks in the hydraulic system (outside and inside the cell), breach of a weak seal at the injection well, and sizable fissures in the rock specimen capable of taking fluid when pressurized by the well. No leaks were detected outside the cell and no damaged areas were observed on the surface of the sample. It was not possible to check for leaks inside the cell or the well seal. Therefore, the test was continued and higher flow rates were used to compensate when required. Visual observations made once the sample was

removed confirmed the idea that the sample contained pre-existing fractures and that these were conductive enough to pass fluid. Blue dye was added to the injection fluid in order to highlight the conductive structures located in the rock matrix while subject to the external constant pressure interval. An immediate result of which was the end of fluid reaching the surface even after pressure was increased to 4 MPa.

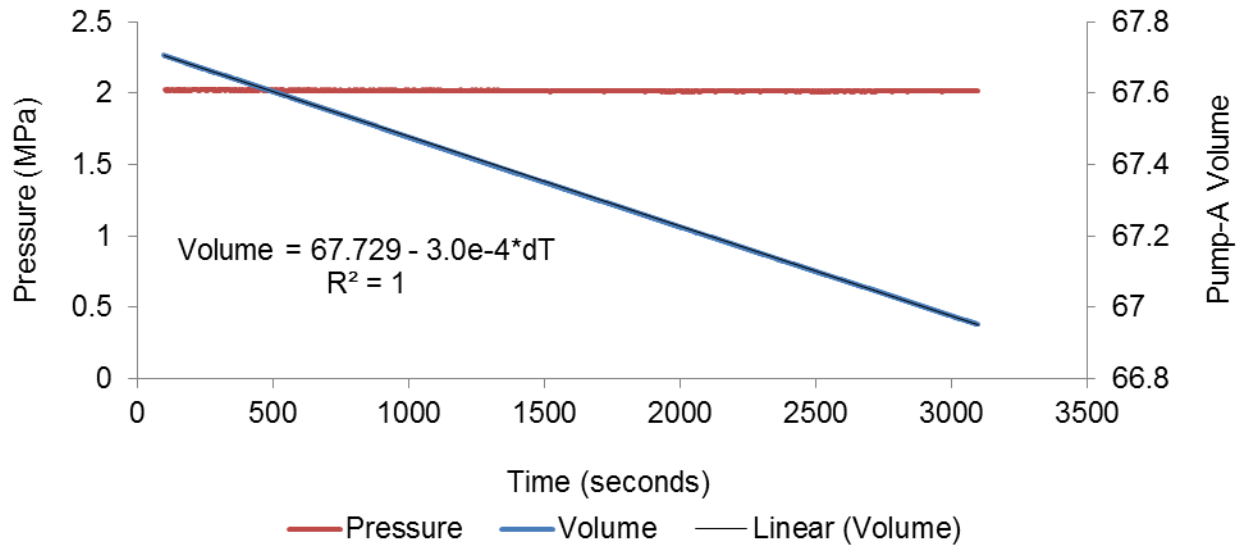


Figure 21: G01-92 Pump-A fluid volume during initial 2 MPa CP interval

3.2.2. Pressure, Strain, and Acoustics

Stimulation began with a flow of 0.05 mL/min and reached a state of equilibrium near 6 MPa. Because pressure did not produce a breakdown event the pumps were stopped until pressure fell below 2 MPa. Flow was increased for trials two and three to 0.1 mL/min and trial four to 0.2 mL/min. The process of stopping pumps, letting pressure decline, and starting a constant pressure stage after reaching equilibrium was repeated for each stage prior to the start of a new stimulation trial. Activity in trial three was significantly reduced compared to the preceding trial but increased once flow was increased to 0.2 mL/min in trial four (Figure 23). One likely cause for this change is the Kaiser phenomena observed in material subjected to repeat loading. Kaiser observed that acoustic activity in cyclically stressed material will be

significantly reduced or nonexistent until stress reaches the maximum historic level. Mogi (2007) made similar observations regarding cyclic bending of granite beams during his studies of acoustics but also observed time dependence to this theory. After extended periods of time activity could nearly recover at pressures lower than historical maximums. Once pressure reached the maximum level experienced in the third trial major activity was reinitiated in trial four (Figure 23). Since trial three reached the same equilibrium point no significant levels of activity were recorded.

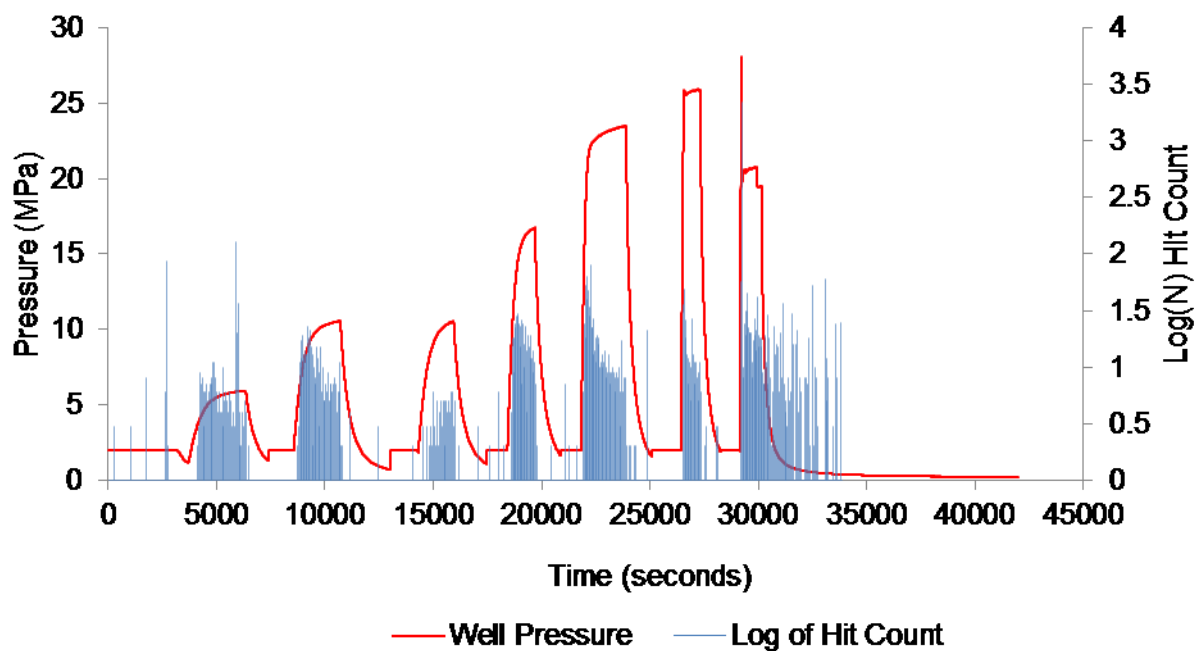


Figure 22: Pressure and log count of hit rates for the first set of stimulation trials

Pressure in stage 2 reached an approximate state of equilibrium 10712 seconds into the test at about 10.6 MPa. Acoustic activity lowered after pumping was stopped and did not reach appreciable levels until pressure reached 10.7 MPa in stage 4 at about 18670 seconds into the test. Figure 24 shows a plot of the pressure reached at the time activity began to show elevated levels plotted against the previous maximum load. The pressure curve in stage 6 indicated that

partial fracture occurred after reaching a peak stress but no significant change in pressure occurred. Stage 7 did experience breakdown.

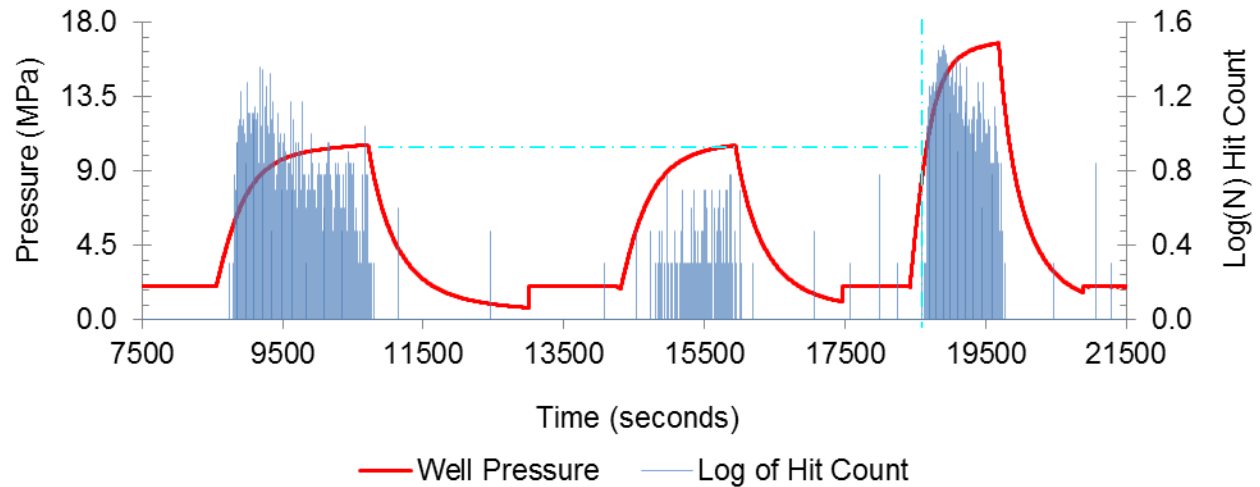


Figure 23: Well pressure and a log count of acoustic activity for stages 2, 3, and 4

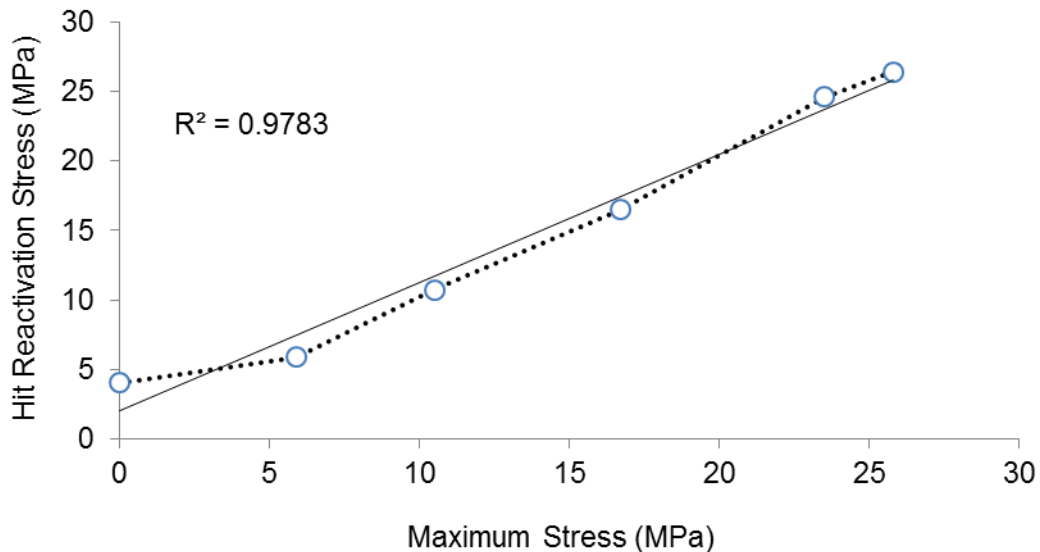


Figure 24: Plot of hit activity reactivation stress against previous maximum stress. Stage 3 is excluded from the trend analysis because of its low level of activity.

The seventh trial contained breakdown and experienced an increase in the level of acoustic emission activity (Figure 22). Additional activity after breakdown was also recorded but at reduced levels. During this time a majority of activity was being collected by sensors 1, 2, and 3 located at the top of the specimen. One likely cause for this preferential collection may have been that the stimulated fracture intercepted the pre-existing fractures early in the stimulation process and carried injected fluid towards the sample surface. Sensors one, two, and three appeared to have either rested near or on a portion of these existing fractures and may have detected large amounts of fluid moving through nearby networks. Energy from these events are likely insufficient to travel to sensors at lower portion of the sample without experiencing significant decay. A constant pressure interval run after the sample was removed from the cell showed many fractures were oriented parallel to the x-axis and extended across much of the y-axis. These fractures were first noticed as injected water reached the top surface after the sample was removed from the cell. These fractures were likely distance from the well and compatible orientations did not indicate these fractures were formed with stimulation treatment but were rather a pre-existing network reactivated during experimentation.

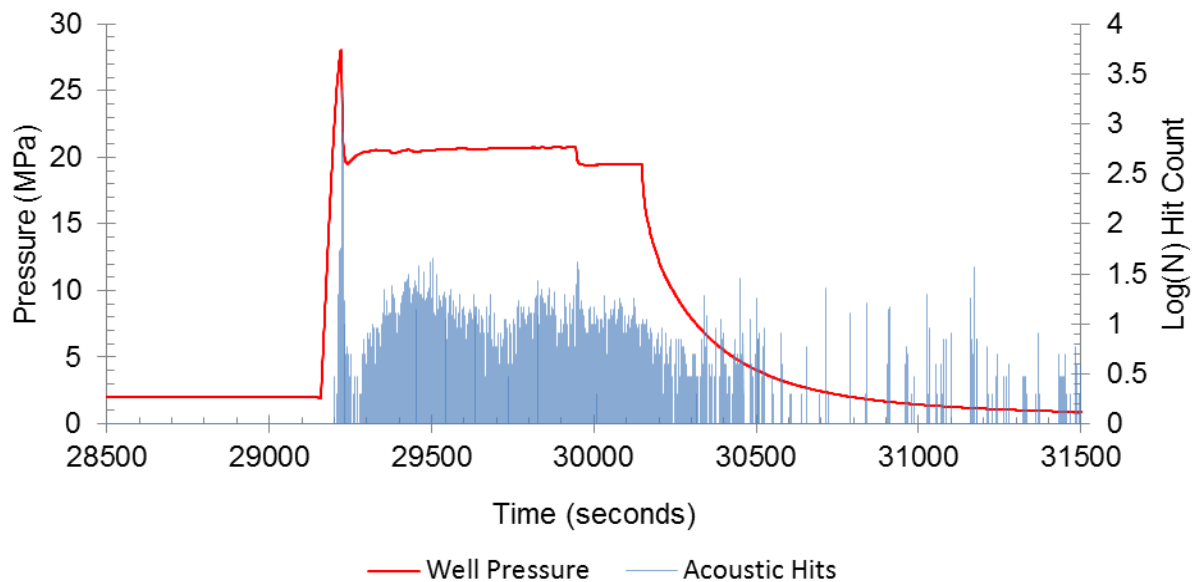


Figure 25: Hit count at the time of breakdown using a constant flow of 1.6 mL/min

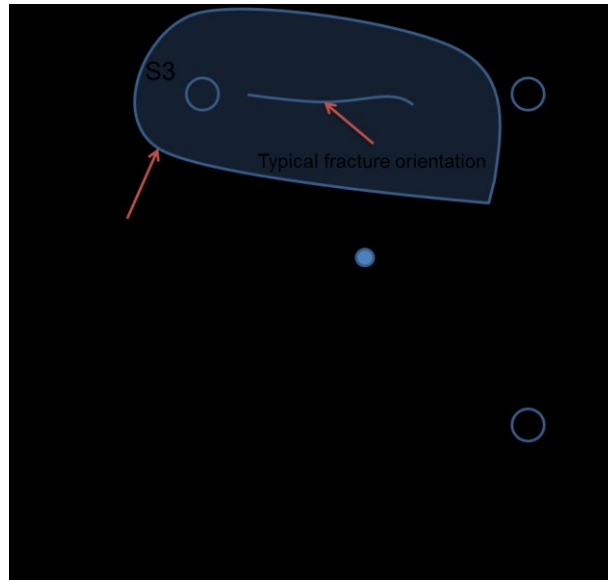


Figure 26: Location of Sensors and Area of Fracture Detection

Strain for G01-92 also changed in accordance to changes in pressure similarly to acoustic data (Figure 27). Strain is plotted with pressure for the interval leading up to and immediately after breakdown. The log value of hit counts is plotted after being normalized and scaled relative to pressure. Some deformation is measured in the sample but is accompanied by relatively low levels of acoustic activity prior to the main breakdown event. At approximately 29220 seconds into the test acoustic activity increases, followed by changes to strain rate and then major pressure decline. Near 29230 seconds into the test acoustic activity declines and the rate of strain reduces. Pressure falloff ends and reaches equilibrium near 20.5 MPa. Hit amplitude is plotted against pressure to highlight the relationship between hit magnitude, the seismic b-value, and pressure level (Figure 28). Increased pressure brings with it increased wave amplitude and therefore increased fracture deformation. However, the seismic b-value does not show the expected sustained drop in activity, and indicates the number of large amplitude events is small relative to low amplitude events. This ratio suggests that fracture was limited in scale and no major extension occurred. It may also be an indication of the narrow range of activity remaining after cyclically loading the sample using constant flow regimes. The

previous trials would have failed the weakest material in steps as flow produced stepwise increases to pressure over time and removed the range of failures expected at breakdown.

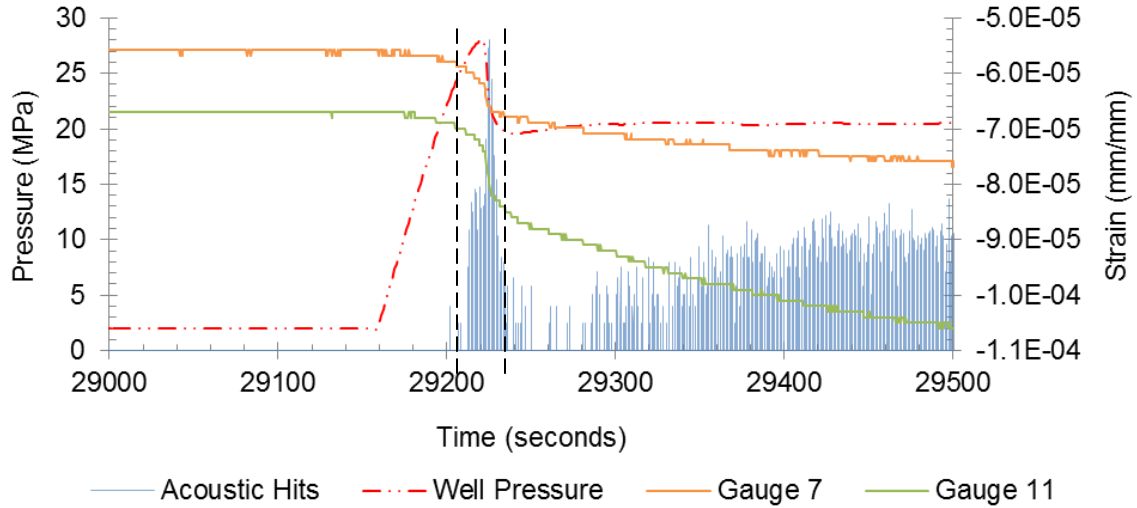


Figure 27: Logarithmic hit counts with pressure and strain at two gauges located on perpendicular faces. Hit counts are normalized relative to pressure. Hits increase at 29220 seconds and fall again at 29230

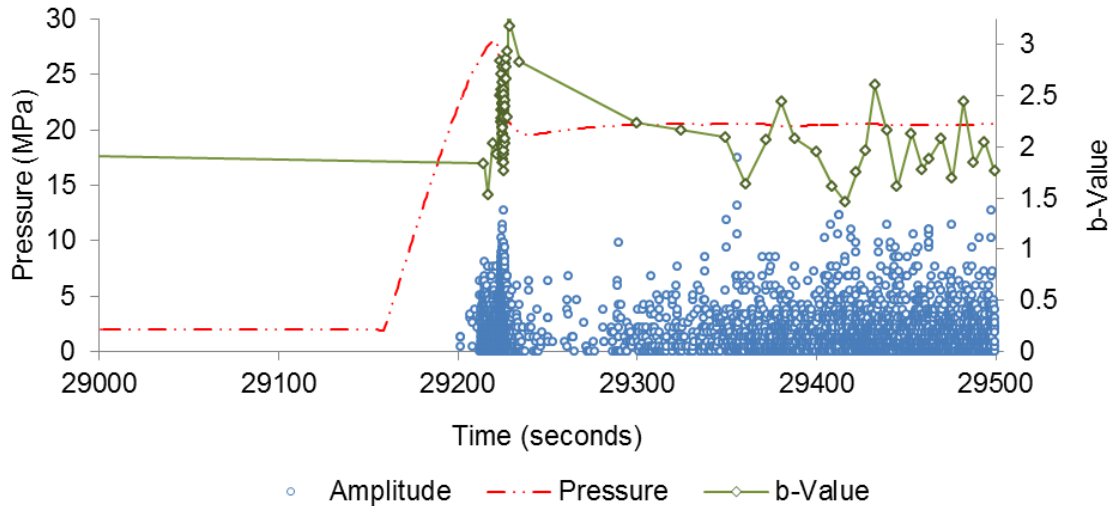


Figure 28: Change in the amplitude spread with time and pressure. The true amplitudes are normalized and scaled against pressure. The amplitudes range between 25 dB (Threshold) and 66 dB (max detected).

3.2.3. *Fracture Geometry*

Filtration was applied to breakdown events in order to isolate the largest amplitude events with the best positional confidence. Events plotted in Figure 29 are sized proportional to maximum amplitude and colored according to error in location estimates. Cool colors (blue) have lower positional confidence and a value approaching 1 while warm colors (reds) have higher confidence and reach a maximum of 10. Using these events, a failure plane was estimated from the relative locations of all events and believed to extend in the x-direction from the well towards the origin. There was also the presence of a slight offset from the injection well. Events located throughout the test have lie on a plane structure that appears to reflect the available flow paths naturally present in the material. Stimulation events are also contained within this general area and suggest that breakdown occurred near the well and fracture growth was highly influenced these existing low resistance flow paths. Likely, the breakdown event gave the well access to these natural fractures and fluid found a lower energy path to flow follow towards the surface than extending a hydraulic fracture. Such preferential flow may explain the large percentage of activity recorded by sensors 1, 2, and 3 since they were located closer to the area of activity near the surface end of the fracture network. Sensor 3 appeared to be located directly on top of this network.

Sample G01-92 was stimulated using water under triaxially confined conditions. Hit counts and amplitudes were used to monitor the stimulation process and event locations were used to source areas of significant damage. Repeated stress cycles created from cyclic fluid flows also created stages in acoustic output that highlighted Kaiser's material stress memory observations. Events did not identify a fracture plane in similar fashion to sample G01-91 but did appear to lie parallel to the direction of pre-stimulation damage. Fluid appeared to be captured by these networks and carried up towards the samples top surface, exciting sensors at

this face. Fluid viscosity increased after the sample was removed from the cell and decreased the fluid flow sufficiently fluid under pressure was no longer able to reach the surface using constant pressures.

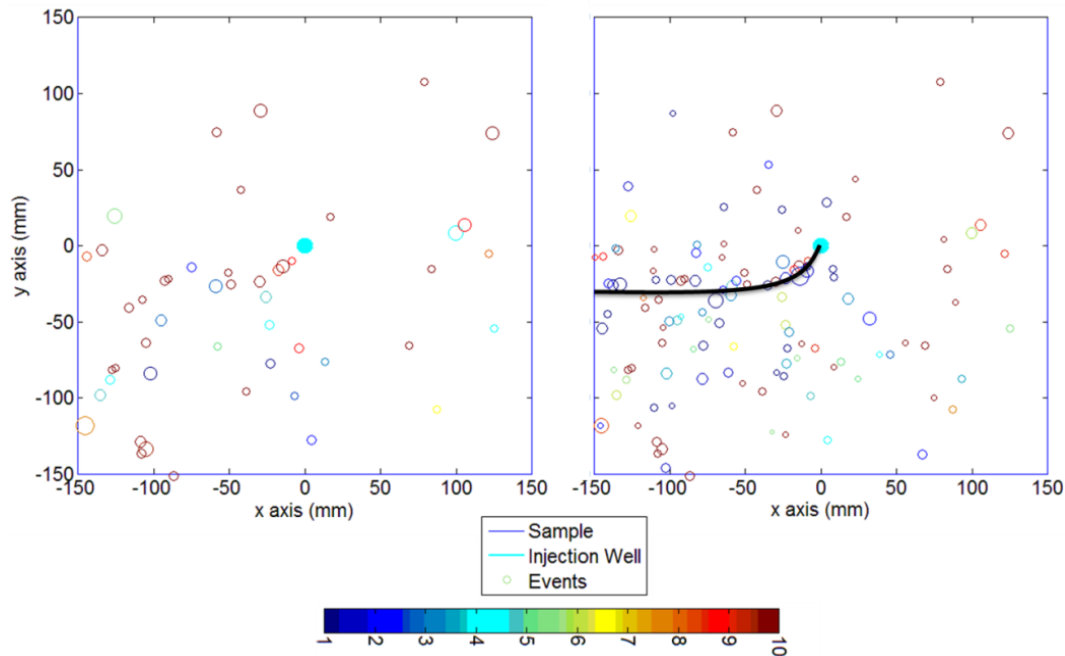


Figure 29: (Left) Events at breakdown (Right) All Events,

3.3. Sample G01-93

Sample G01-93 was an EGS test comprised of an injection well and two production wells. The injection well was placed at 15 degrees off vertical and reached a vertical depth of 150 mm into the sample (Figure 30). Drilling occurred in two stages with the first being lined with 3/8 inch (~10 mm) steel casing and the second left uncased for stimulation. The first and second stages reached a depth of 100 and 50 mm, respectively, and contained internal well diameters of 2/8 inch (~6 mm). Production wells drilled into the sample remained uncased for fluid extraction. A 30 degree tilt was used to optimize the likelihood a production well would intercept stimulated fractures during placement. Each production well was placed according to event locations and with a minimum 50 mm linear distance from the injection well to minimize

interaction between producer and injector and provide maximum flow path distance. Confining stress included a minimum horizontal, maximum horizontal and vertical stress of 4, 8, and 13 MPa respectively. Stimulation was completed using oil and proppant and reached a maximum breakdown pressure of 31 MPa. Stepped constant pressure (CP) and stepped constant flow (CF) tests were used to estimate permeability of the induced fracture network and analyzed to measure to the effectiveness of treatment. A maximum flow rate of 6.4 ml/min was reached during the last stepped constant flow test. Blue dye was placed in the injection fluid at this stage to highlight fluid paths created during stimulation treatments. In all, a total of 5 stimulation treatments, 48 stepped constant pressure tests, and 5 stepped constant flow tests were completed to measure permeability and obtain temperature drawdown measurements with flow. Acoustic monitoring occurred during all stages and was a beneficial addition to traditional tools for monitoring sample behavior during treatment.

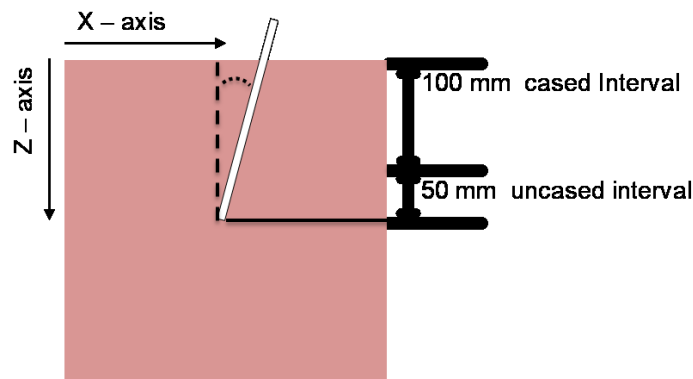


Figure 30: Example of angled injection well (white) with approximate depth dimensions

Monitoring of EGS G01-93 started with sample preparation and continued through stimulation, re-stimulation, and pressurization through stepped constant pressure and flow intervals. A threshold level of 32 dB was used during the initial stages of testing. Initial acoustic measurements of velocity and attenuation were taken outside the cell using auto sensor and pencil-lead break tests with acoustic sensors fixed using silicone caulk. Additional measurements of wave velocity and attenuation were taken once the sample was placed inside

the cell using the AST procedure (Table 4). Acoustic monitoring conducted during the confining and heating stages produced significant activity and located several events. The high levels of activity confirmed that the system was recording properly. No areas of weakness were identified and confinement did not induce damage that was thought to influence the fracture process.

Table 4: List of G01-93 acoustic properties

Test Stage	AST Velocity (mm/s)	PLB Velocity	Attenuation (dB/m)	PDT (μ s)	HDT (μ s)	HLT (μ s)
Out of Cell	3.5×10^6	4.2×10^6	82	100	200	2
In Cell	3.2×10^6	N/A	133	100	200	2

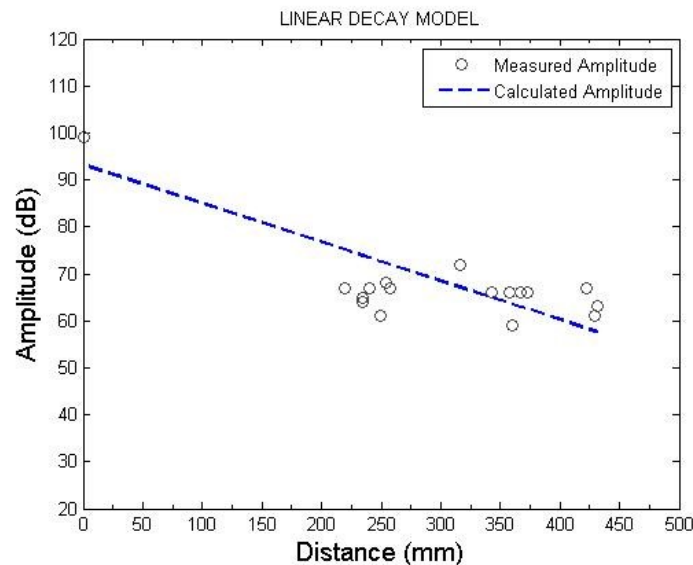


Figure 31: Plot of out of cell attenuation and in cell attenuation for G01-93,

3.3.1. Acoustics and Pressure

Acoustic activity occurred in two distinct stages during the loading process (Figure 32). In the first observable stage output is relatively constant with time and increasing pressure. The continuous production of hits and the early drops in pressure while loading process suggested

the creation or reactivation of fractures prior to the development of a hydraulic fracture at breakdown. These hits were believed to occur in areas of weakness where complex stress regimes or existing fractures were activated by the loading process. Continuous activity and increasing pressure suggested the activity being generated have limited interaction with one another and have not coalesced into significant macro fractures. A second stage shows quickly increasing levels of hit activity as pressure reaches breakdown levels. The significant pressure drop and spike in activity suggest breakdown occurred with fracture coalescence and extension into the sample. Association with breakdown activity coupled with the observation that events created during this time were normal to the minimum principal stress suggest a tensile type failure and generation of new fracture surfaces based on elastic fracture mechanics theory. Stimulation lasted approximately 3.5 hours (14,000 seconds) and experienced 3 pressure build up and breakdown stages (Figure 32). Each stage is accompanied by increases in activity prior to pressure drops, showing damage evolution with changing pressure. However, the total amount of activity decreased considerably after breakdown. While low in frequency, activity prior to breakdown consisted of a considerable percentage of total output.

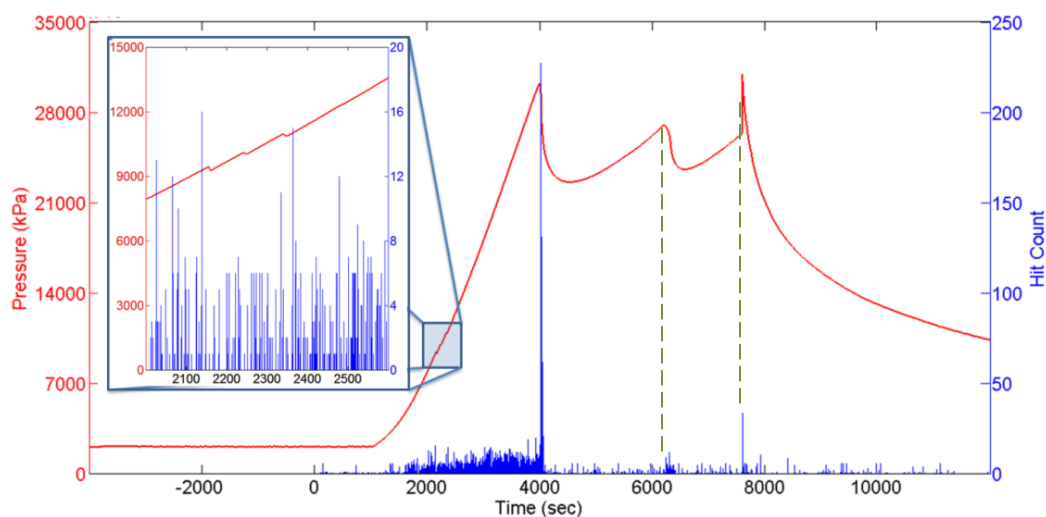


Figure 32: Hit count histogram of stimulation one plotted with pressure

A re-stimulation program was initiated after several borehole swabs and constant pressure trials showed that borehole connectivity was lower than ideally preferred. These programs consisted of additional constant flow tests. Pressure during these stages fluctuated but low levels of acoustic activity suggested that significant damage was limited. As a result, significant fracture extension was not believed to have occurred. Activity spiked with the first two pressure drops in Figure 33, but remained low for the duration of the stimulation test.

In addition to the fracture stimulation tests, a staged constant flow test was conducted with a starting flow of 0.05 mL/min and ending at 6.4 mL/min (Figure 34). Here, a plot of pressure and acoustics are presented during. Several noticeable spikes in the pressure data are observed during this stage at increasing frequency as the test continues (the first black arrow) and result when one pump empties and the second takes over the flow process. One area of interest occurs at time 2.283×10^6 seconds. At this time a blue dye was mixed with the injection fluid to highlight internal fracture networks and resulted in an increase in pressure and acoustic activity (marked by the third black arrow). The increases suggest adding the dye increased the fluid's ability to induce mechanical failure in the matrix and create additional damage. Earlier states of flow and pressure eventually reached some type of equilibrium and were relatively inactive. This likely resulted from already existing fluid paths accepting a majority of the fluids and preventing additional damage. Increasing the fluid viscosity would reduce this capacity by requiring additional force to move the fluid through smaller discontinuities, increasing the force experienced directly by the surrounding matrix, and increasing the probability of inducing damage.

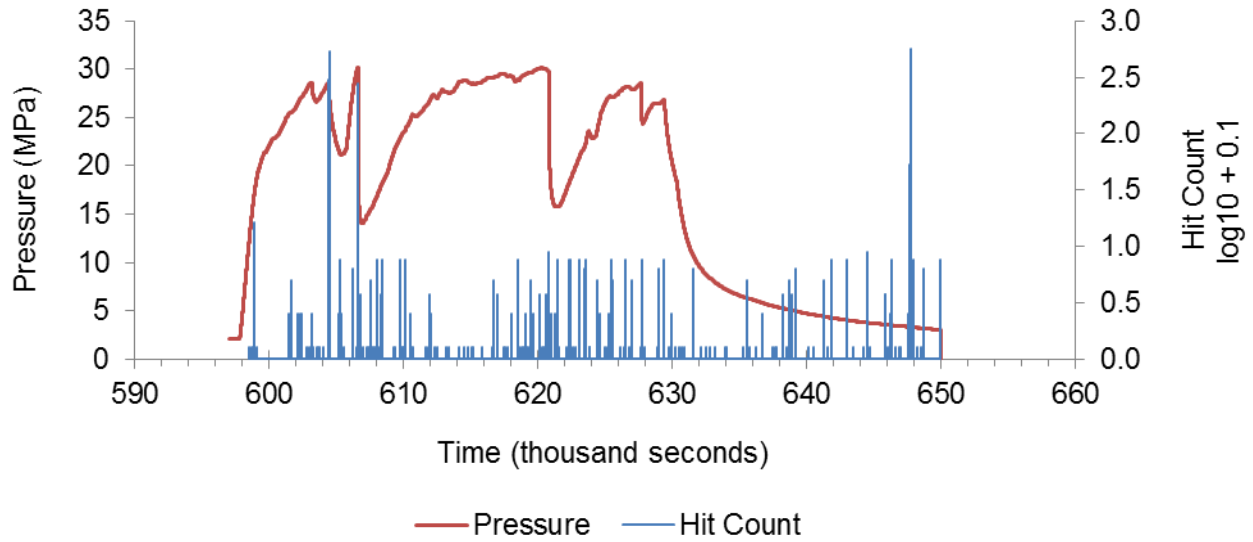


Figure 33: Log-scaled hit histogram from the first re-stimulation test.

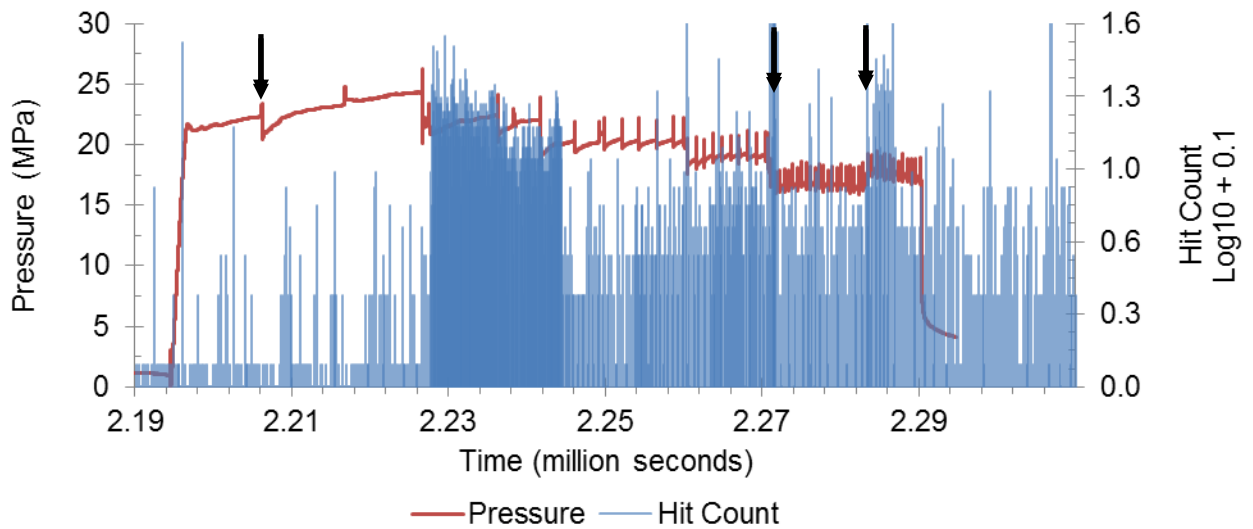


Figure 34: Pressure from constant flow tests. Flow between $2.27 - 2.29 \times 10^6$ sec is 6.4 mL/min. The left arrow shows pressure spike due to pump change and the right arrow show the time when dye was added to the injection fluid.

3.3.2. Fracture Geometry

The spatial distribution of source locations provides an important tool for analyzing damage zones induced by stimulation and was the fundamental basis for positioning production

wells after treatment. The sample presented in Figure 35 shows relative locations of the injection well and filtered events associated with the first stimulation procedure from initial pressurization to pump shut off. Events extend several tens of millimeters away from the well in two distinct directions. First, events from the loading stage form an inclined plane extending at an angle between the maximum and minimum horizontal confining stress (Figure 35). Pressure drops experienced during the loading procedure suggested these events were associated with limited reactivation of pre-stimulation fractures on a previously damaged plane similar to that of sample G01-92. The injection well outline is identified in cyan lying near the center of the sample. Filtered events are presented with increasing size representing increasing amplitude. The colors represent increasing confidence in measured location. A confidence of 1 represents a correlation of 0 and no confidence in event localization whereas a value of 10 represents a correlation of 1 and low error in the estimate.

Events were filtered by removing the bottom 25 percent based on amplitude. Of these, the top half of events based on location correlation was kept to remove weak events with no spatial confidence from analysis. The positive x-direction was used as a reference plane when examining event distribution and clustering. Results from this filtration show most significant events were located in the initial plane created during pressurization. Events along this plane extend at an angle approximately 200 degrees from the positive x-direction (Figure 36). The second group of events created during breakdown lied approximately 90 degrees from the positive x-direction and were normal to the minimum principal stress (positive y-direction). This direction agrees with linear elastic fracture mechanics theory for a fracture stimulated with differential lateral stresses. In addition, a significant majority of all events are located between the bottom of the injection well and the top of the sample. Few events extend toward the bottom of the sample, especially in the hydraulic fracture.

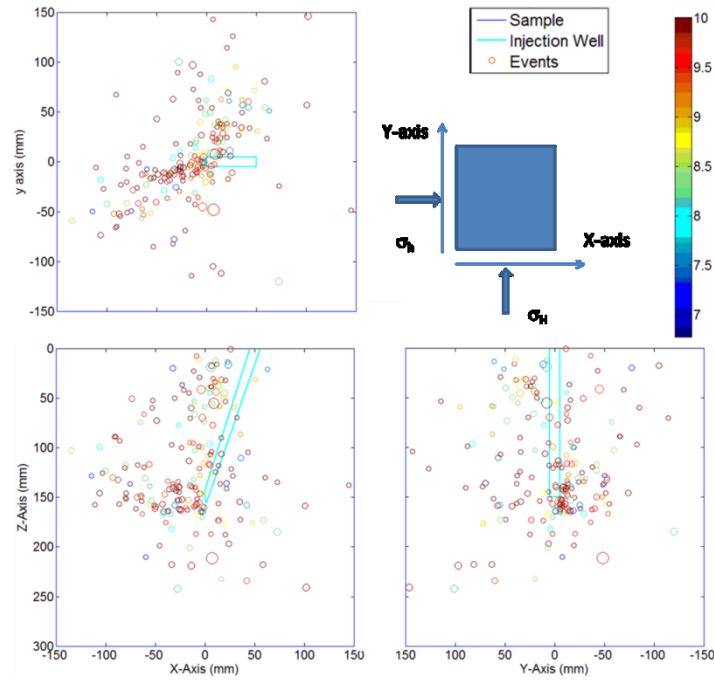


Figure 35: Filtered event locations

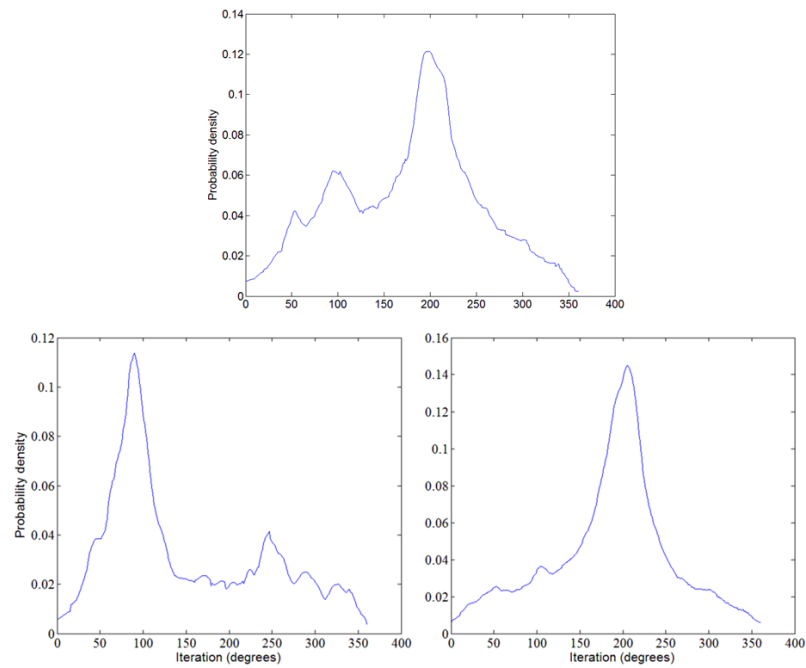


Figure 36: Centered Top – Density for all filtered events. Bottom Left – Density for filtered events at breakdown. Bottom Right – Density for filtered events prior to breakdown

3.3.3. Post Stimulation Flow

Production wells were drilled into the sample based on the highest density of events produced during stimulation. The goal of each well was to intercept the fracture network while minimizing stress interactions between one another and maximizing the flow path between wells. To accomplish this each well was placed a minimum of 5 well diameters, or approximately 50 mm, linear distance from the injection well. Well 1 was placed in the location believed to be formed from tensile separation theoretically associated with the creation of hydraulic fractures. A majority of these events were located between the bottom of the injection well and the top of the sample. The second well was placed in the band of events believed to be associated with fracture reactivation or failure of weak material within the matrix during initial pressurization. The greatest concentration of events associated with this fracture is near the bottom of the injection well and formed the interception target depth (Figure 37). After both wells were placed a pair of constant pressure tests was conducted to estimate conductivity of the newly formed fracture. Well 1 contained trace amounts of detectable oil residue on several occasions when conducting internal wipes of the well bore. This suggested interception was successful but connectivity was low. Well 2 did not contain any oil residue, which was interpreted as an unsuccessful interception. Because of the low level of permeability after initial stimulation and lack of connection with well two it was decided to conduct additional treatments to improve fracture conductivity. Total activity during re-treatment was reduced from the initial treatment and only a few events were located. Re-stimulation programs were also unsuccessful in connecting the injection and second production well and it remained unproductive through the completion of testing. Pressure during this time remained highly variable and elevated which was interpreted as activity within a sample confined fracture. The low levels of activity did not indicate that new damage was being initiated and fracture substantial fracture growth was unlikely.

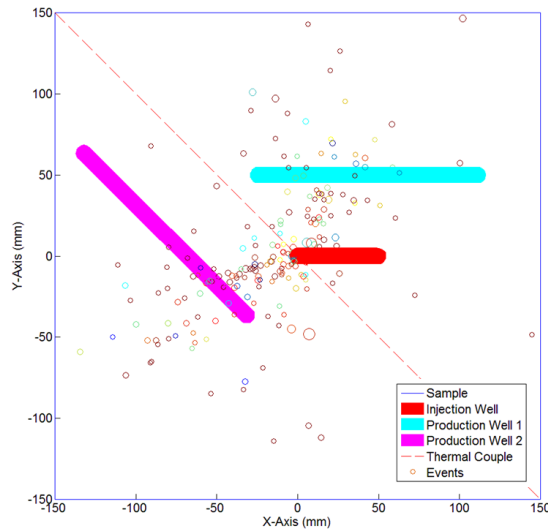


Figure 37: Production well placement using event densities to estimate fracture geometry

The sample was removed from the triaxial cell for additional analysis after completing treatment. The steel injection well was over cored and the sample was sent to a local private rock cutting company to be sectioned into 25 mm thick slices which were visually reviewed to examine internal fracture geometries and make comparisons with acoustic data. One observation from the sections was the interception of production well 2 with a secondary band of material located near its bottom. Three slices were chosen to obtain measurements of the band inside the section with three dimensional coordinates. The first slice, located at $z = 128$ mm depth was located above the last section of production well 2. The second slice was located at $z = 154$ and contains the last length of production well 2 within the sample. It is also the depth where the production well intercepted the discontinuity. The last slice lies at $z = 179$ mm and is located directly beneath the second and contains no portion of well 2. This slice also contains the last section of drilled material for the injection well. The right boundary of the secondary material band is often less distinct than the left boundary and occasionally appears to fade into the general matrix. Approximately 50 % of the events produced during stimulation lie between the 49 mm bound by all three sections. They are also closely aligned with the approximate location of the band (Figure 39).

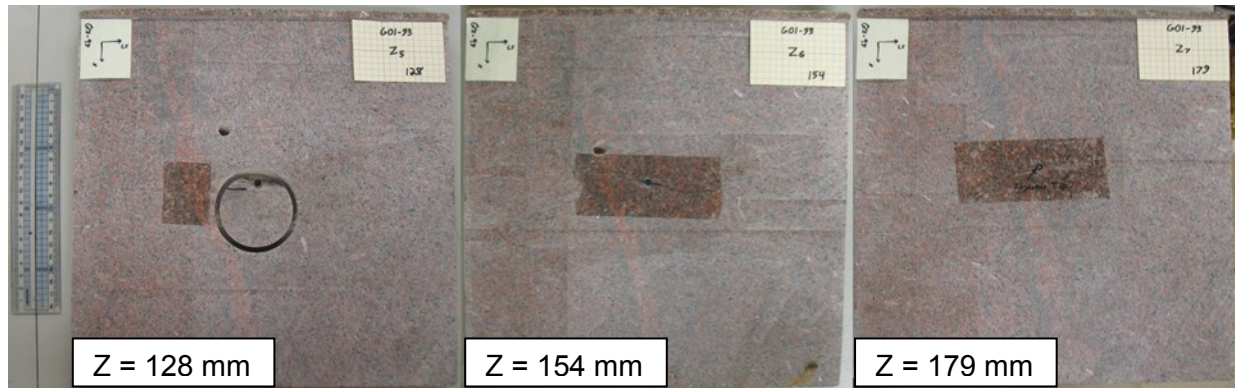


Figure 38: Slice 1, 2, and 3 of the plotted discontinuity band. The center contains production well interception.

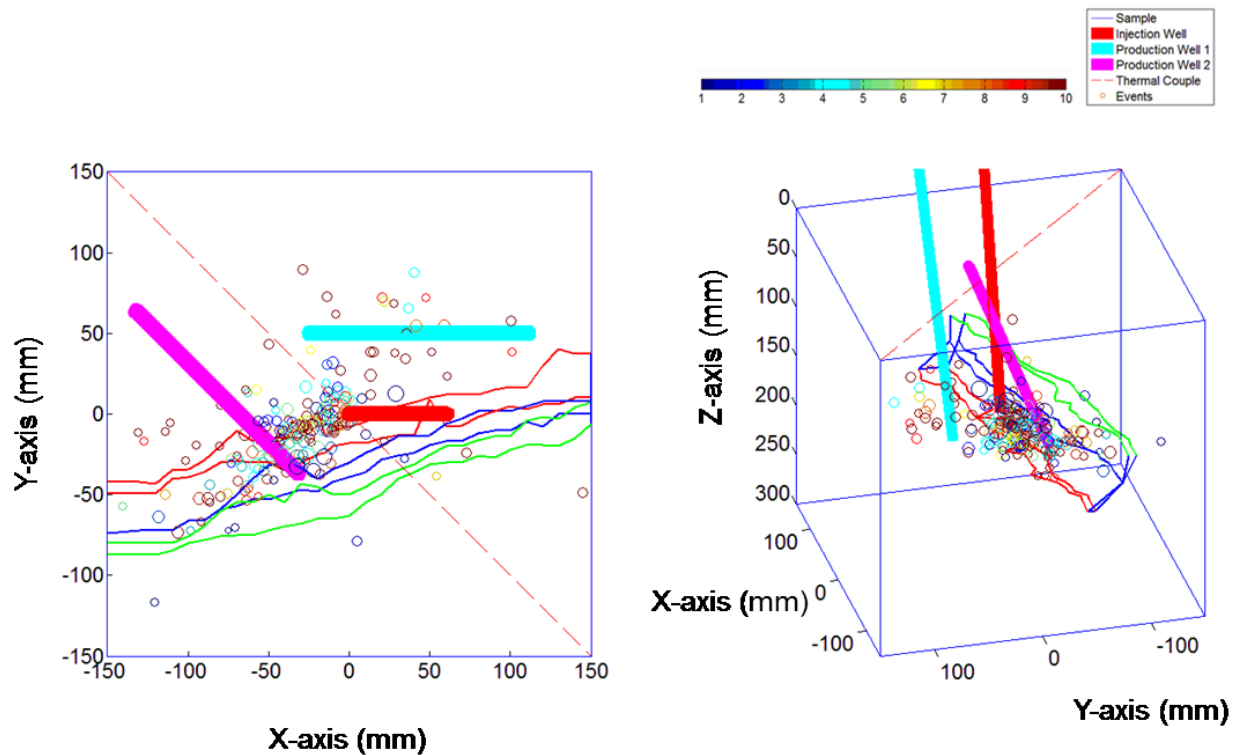


Figure 39: Plot of events with discontinuity envelope. Slice 1 (top) is colored green, slice 2 (middle) is blue, and slice 3 (bottom) is red. Locations are near the discontinuity.

Sample G01-93 was heated, triaxially confined, and stimulated using SAE 80W-90 gear oil. Rock temperature ranged from 85 degrees at the sample bottom to 75 degrees at the sample top. Thermally insulating bricks were used to maintain a constant temperature during

the duration of the test. Stimulation resulted in two distinct acoustic clouds that were intercepted with production wells for fluid flow testing. Both wells were successful in reaching their desired location but only one was successfully connected to the injection well via fracture. After inspecting the sample slices a noticeable band of secondary material was observed in the vicinity of events localized during testing. The band was likely the source of these events and supports the interpretation that events and activity during initial pressurization occurred from localized failure in the material (e.g. stress concentration) and were not part of the fracture development phase. Production well 1, created at breakdown, was connected by an internal fracture network sufficient to carry large volumes of water from the injection well. Pressure declines experienced during initial loading were likely a result from the creation of small but limited fractures near the well. Changing the fluid viscosity had an evident impact on fluid flow through the fracture. Pressure and acoustic activity both increased once the new mixture reached the sample.

4. SUMMARY AND CONCLUSIONS

4.1. *Summary*

Three granite specimens were hydraulically stimulated with epoxy, water, and proppant-laden oil. These samples were monitored using acoustic emission technology in order to observe fracture dimensions and perform a complete fracture analysis. Wave properties including velocity and attenuation were measured during each test in order to obtain the sample-specific values necessary for robust source location and amplitude correction. This analysis was required because of the random nature of each specimen's composition. Variation resulted in unique stimulation behavior regardless of the similar place of origin for all three samples. Fracture locations were identified from acoustic clouds produced during stimulation treatment through event filtration and density measurements. These locations were then used to identify the best regions for production well placement and to identify damage within the material. Events located within filtered windows of time were further used to identify fractures associated with hydraulic fracture. Fracture stages were identified through total hit activity and changes to amplitude spread over time. Influence of injection fluid viscosity on the fracture process was documented based on differences of breakdown behavior among samples as well as the acoustic response of an individual sample exposed to injection fluids of different viscosity in a single flow stage.

4.2. *Conclusions*

In conclusion, acoustic emission technology provides important tools to monitor fracture within geologic materials subject to hydraulic stimulation. Source location and filtering techniques enable accurate production well placement to enhance stimulated fracture

interception and optimize reservoir access. Moreover, a combination of hit rates and amplitude distribution over time can be used to successfully monitor changes in the fracture process that complement observed fluctuations in material strain, well pressure, or other methods of damage assessment. Together these items provide a more holistic approach to conducting laboratory research on fracture propagation from a variety of load scenarios.

The presence of viscous fluids has a major impact on the fracture process. During these tests, samples subjected to higher viscosity fluids showed elevated breakdown pressures, increased damage, and larger fracture dimensions than samples stimulated with lower viscosity fluids. The presence of natural fractures reduced flow resistance and increased fluid loss from the fracture when using relatively low viscosity water as a stimulation fluid. Pre-stimulation fractures likely reduced internal fracture pressure and limited local damage. Use of a viscous fluid may increase the fluids resistance to permeate intercepting discontinuities and maintain elevated pressure across the fracture face. Sample G01-92 contained many pre-stimulation discontinuities first observed when water reached the surface of the unconfined sample near the acoustic sensors. Hair dye added to the injection fluid the injection fluid increased the fluid viscosity and resulted in decreased flow. No fluid reached the surface at pressures up to 4 MPa. Likewise, sample G01-93 experienced increased acoustic activity when dye was mixed with water and injected into the sample. One possible conclusion taken from these two examples is the reduced permeability prevents fluid loss from the fracture, increases the internal pressure along the fracture face, and therefore increases the likelihood of inducing substantial failure. Sample G01-91 contained the most viscous injection fluid of the three injections and also resulted in the most distinct fracture. The fracture created at breakdown was a bi-wing, planar fracture that was extended from the well to the 3 of faces of the sample. Breakdown with this sample was accompanied by significant acoustic activity and indicates a significant amount of major fracture extension relative to 92 and 93.

Geometric event distributions can be used to successfully estimate relative extent and severity of damage induced through stimulation. However, the presence of high intensity events and large clusters do not necessarily indicate connected fracture networks. With the exception of G01-92, only fractures induced during breakdown were associated with connected flow paths. Additional zones identified as high density areas and contained large amplitude activity did not contain connected flow paths sufficient to carry fluid from the well and are likely a result of localized damage in highly stressed zones or near irregular material boundaries. In the case of G01-91, a band of material distinctly different than the main rock matrix contained a large number of events created prior to breakdown. The relative amplitudes of these events were similar to many of those that rested on the final fracture plane estimated from event density after filtration. However, these events contained no major visible fracture similar to the breakdown hydraulic fracture. Similarly, G01-93 produced events limited to clouds in two distinct planes during stimulation. Filtration based on amplitude showed that events were of comparable magnitude along each plane and lead to the possibility of two distinct fracture surfaces. However, only the events associated with the assumed hydraulic fracture created at breakdown produced a conductive well. No observable fractures could be identified along the path of these events and they likely occurred due to granular interactions created by the complex stress regime of an oriented well. Events in G01-92 created prior to breakdown were also likely associated with pre-stimulation discontinuity. The event cloud produced during stimulation laid in the same orientation as the pre-stimulation events and likely resulted from capture of the stimulation fluid once they intercepted hydraulic fracture. However, not all areas were identified by events and flow outside of this identified region did occur, as indicated by heightened activity at particular sensors. Overall, activity associated with the breakdown curve and the theoretical extent of the tensile hydraulic fracture are more likely to be conductive than planes identified by intensity or density alone.

4.3. *Recommendations for Future Studies*

Additional research to highlight fractures with the highest likelihood of producing major flow paths is required to optimize the location of geothermal production wells and increase effectiveness of treatment procedures. Enhanced theory on the initiation and propagation of fractures could also be useful for designing treatments prior to stimulation. The rate of captured activity and magnitude of waveforms are also strong indicators of a materials response changes in loading. This can be beneficial for mapping stress histories within limited window of time, assessing the likelihood of inducing additional damage, and possibly as a predictive measure against failure. Acoustic emission is a well-accepted and powerful tool, and is a strong compliment other traditional methods of laboratory measurement. However, it is limited in its predictive capacity relative to newly developed numerical models and fracture development tools currently being developed to estimate fracture behavior prior to loading. Nonetheless, its ability to map fracture stages and locations, measure displacement modes and volumes, and to capture waveforms are beneficial measurements that can be used to confirm these models.

5. APPENDIX

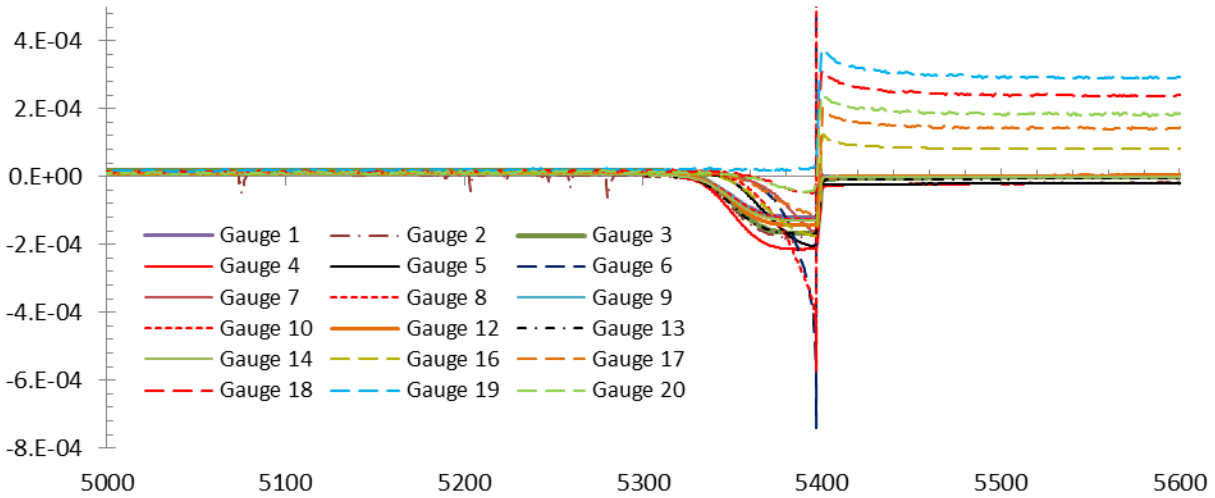


Figure 40: All strain gauges for G01-91

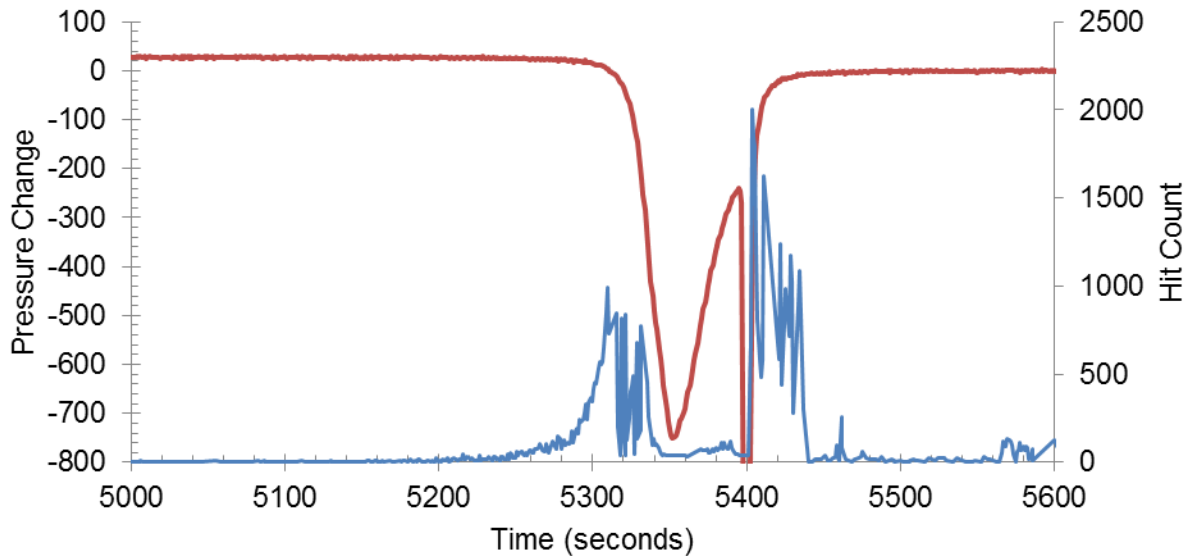


Figure 41: Acoustic hit counts and pressure derivatives at breakdown. Maximum pressure change exceeded the charge scale by a factor of 8, reaching nearly -6.5 MPa in the tertiary stage.

6. WORKS CITED

- Aggelis, D.G., D.V. Soulioti, N. Sapourdis, N.M Barkoula, A.S. Paipetis, and T.E. Matikas. "Acoustic emission characterization of the fracture process in fibre reinforced concrete." *Construction and Building Materials* 24 (2011): 4126 – 4131
- Aki, K., and P. Richards. *Quantitative Seismology*. Mill Valley, California: University Science Books, 2002.
- Aki, K., "Maximum likelihood estimate of b in the formula $\log N = a - bM$ and its confidence limits." *Bulletin of the Earthquake Research Institute* 43(1965): 237-239
- Albright, J., and C. Pearson. *Society of Petroleum Engineers* 22, no. 4 (1982): 523-530.
- Al-Bushaidi, A., J.F. Hazzard, and R.P. Young. "Distinct element modeling of hydraulically fractured Lac du Bonnet granite, J. Geophys. Rs., 110, no. B6 (2005): 1-14
- Annual energy review 2011. 2012. [S.I.]: U S Govt Printing Office.
- Bates, C.R., H.B. Lynn, M. Simon. "The study of a naturally fractured gas reservoir using seismic techniques." *AAPG Bulletin* 83, no. 9 (1999): 1392-1407.
- Benson, P.M., Thompson, B.D., Meredith, P.G., Vinciguerra, S., R.P. Young. "Imaging slow failure in triaxially deformed Etna basalt using 3D acoustic-emission location and X-ray computed tomography." *Geophysical Research Letters* 34 (2007): 1-5
- Carter, B., J Desroches, and P. Wawrzynek. "Simulating fully 3D hydraulic fracturing." *Modeling in Geomechanics*, 200: 525-557.
- Dahm, T. "Relative moment tensor inversion based on ray theory: theory and synthetic tests." *Geophysical Journal International* 124, no. 1 (1996): 245-257.
- Daniel, G., and J. White. "Fundamentals of Fracturing." *Society of Petroleum Engineers*, 1980: 1-8.
- Frash, L., "Laboratory stimulation of an enhanced geothermal reservoir." M.S. thesis. Colorado School of Mines, Department of Civil and Environmental Engineering (2012)
- Fisher, M.K., C.A. Write, B.M. Davidson, A.K. Goodwin, E.O. Fielder, W.S. Buckler, and N.P. Steinsberger. "Integrating fracture mapping technologies to optimize stimulations in the Barnett Shale." *Society of Petroleum Engineers* (2012): 1-7.
- Ge, M., "Analysis of source location algorithms Part II: Iterative methods." *Journal of Acoustic Emission* 21 (2003): 29-51
- Geiger, L. "Herbsetimmung bei erdbeben aus den Ankunftszeiten." *K. Gessel. Wiss. Goett.* 4 (1910): 331-349.
- Geiger, L. "Probability method for the determination of earthquake epicenters from the arrival times only." *Bulletin of St Louis University* 8 (1912): 60-71.

- Gutenberg, B., C. Richter. "Frequency of earthquakes in California." *Bulletin of the Seismological Society of America* 34 (1944): 185-188
- Hampton, J. "Laboratory hydraulic fracture characterization using acoustic emission." M.S. thesis, Colorado School of Mines, Department of Civil and Environmental Engineering (2012)
- Haring, M. Ulrich, S., Ladner, F., Deyer, B., "Characterization of the Basel 1 enhanced geothermal system." *Geothermics* 37, no. 5 (2008): 469-495
- Hazzard, J.F., R.P. Young, and S.C. Maxwell. "Micromechanical modeling of cracking and failure in brittle rocks." *J. Geophys. Res.* 105, no. B7 (2000): 16683-16697
- Ishida, T. "Acoustic emission monitoring of hydraulic fracturing in laboratory and field." *Construction and Building Materials* 15 (2001): 281-295.
- Ishida, T., Q. Chen, Y. Mizuta, and J. Roegiers. "Influence of fluid viscosity on the hydraulic fracturing mechanism." *Journal of Energy Resource Technology* 126, no. 3 (2004): 190-200.
- Ishida, T., Aoyagi, K., Chen, Y., Murata, S., Chen, Q., Nakayuma, Y. "Acoustic emission monitoring of hydraulic fracturing laboratory experiment with super critical liquid CO₂" *Geophysical Research Letters* 39 (2012): 1-6.
- Johnston, D.H., M.N. Toksoz, and A. Timur. "Attenuation of seismic waves in dry and saturated rocks: II. Mechanisms." *Geophysics*. 44, no. 4 (1979): 691-711.
- Kao, C. S., F.C.S. Carvalho, and J. F. Labuz. "Micromechanisms of fracture from acoustic emission." *International Journal of Rock Mechanics and Mining Sciences* 48, no. 4 (2011): 666-673.
- Lei, X., K. Kusunose, M.V.M.S. Rao, O. Nishizawa, and T. Satoh. "Quasi-static fault growth and cracking in homogeneous brittle rock under triaxial compression using acoustic emission monitoring." *Journal of Geophysical Research* 105, no. B3 (2000): 6127-6139.
- Lei, X., O. Nishizawa, and K. Kusunose. "Fractal structure of the hypocenter distributions and focal mechanism solutions of acoustic emission in two granites of different grain sizes." *Journal of Physics of the Earth* 40, no. 6 (1992): 617-634.
- Lockner, D. "The Role of Acoustic Emission in the Study of Rock Fracture." *Int.J. Rock Mech. Min. Sci. & Geomech* 30, no. 7 (1993): 883-889.
- Lockner, D., and J. Byerlee. "Hydrofracture in Weber sandstone at high confining pressure and differential stress." *Journal of Geophysical Research* 82, no. 14 (1977): 2018-2026.
- Majer, E., and T. Doe. "Study of hydrofractures by high frequency seismic monitoring." *International Journal of Rock Mechanics and Mining Sciences & Geomechanics Abstracts* 23, no. 3 (1986): 185-199.
- Manthei, G., J. Eisenblatter, and T. Dahm. "Moment tensor evaluation of acoustic emission sources in salt rock." *Construction and Building Materials* 15, no. 5-6 (2001): 297-309.
- Massachusetts Institute of Technology. *The Future of Geothermal Energy*. Boston: Massachusetts Institute of Technology, 2006.

- Matsunaga, I., H. Kobayashi, S. Sasaki, and T. Ishida. "Studying hydraulic fracturing mechanisms by laboratory experiments with acoustic emission monitoring." *International Journal of Rock Mechanics and Mining Sciences & Geomechanics Abstracts* 30, no. 7 (1993): 909-912.
- Maxwell, S. "What does microseismic tell us about hydraulic fracture deformation." *Recorder* 36, no. 8 (2011): 30-45.
- Meglis, I.L., T.M. Chows, and R.P. Young. "Progressive microcrack development in tests on Lac du Bonnet granite-I. Acoustic emission source location and velocity measurements." *International Journal of Rock Mechanics and Mining Sciences and Geomechanics Abstract* 32, no. 8 (1995): 741-750.
- Michlmayr, G., Cohen, D., Or, D., "Sources and characteristics of acoustic emissions from mechanically stressed geologic granular media – A review." *Earth-Science Reviews* 112, no. 3-4 (2012):97-114
- Mogi, K., "Study of elastic shocks caused by the fracture of heterogeneous materials and its relations to earth quake phenomena." *Bulletin of the Earthquake Research Institute* 40, no. 1 (1962): 125-173.
- Mogi, K., *Experimental Rock Mechanics*, London: Taylor & Francis, 2007
- Moriya, H., T. Fujita, N. Niitsuma, J. Eisenblatter, G. Manthei. "Analysis of fracture propagation behavior using hydraulically induced acoustic emissions in the Bernburg salt mine, Germany." *International Journal of Rock Mechanics and Mining Sciences.* 43 (2006): 49 – 57).
- Niitsuma, H., N. Chubachi, and M. Takanohashi. "Acoustic emission analysis of a geothermal reservoir and its application to reservoir control." *Geothermics* 16, no. 1 (1987): 47-60
- Ohtsu, M. "Simplified moment tensor analysis and unified decomposition of acoustic emission source: Application to in situ hydrofracturing test." *Journal of Geophysical Research* 96, no. B4 (1991): 6211-6221.
- Ohtsu, M., and K. Ono. "AE source location and orientation determination of tensile cracks from surface observations." *NDT International* 21, no. 3 (1988): 143-150.
- Ohtsu, M., M. Shigeishi, and Y. Sakata. "Nondestructive evaluation of defects in concrete by quantitative acoustic emission and ultrasonics." *Ultrasonics* 36 (1998): 187-195.
- O'Connell, R., and B. Budiansky. " Seismic velocities in dry and saturated cracked solids." *Journal of Geophysical Research* 79, no. 35 (1974): 5412-5426
- Pollock, A. A., "Acoustic emission – 2 Acoustic emission amplitudes." *Non-Destructive Testing*, (1973): 264-269.
- Prugger, F.A., and D. Gendzwil. "Microearthquake location: A nonlinear approach that makes use of a simplex stepping procedure." *Bulletin Seismological Society of America* 78, no. 2 (1988): 799-815.
- Reches, Z., and D. Lockner. "Nucleation and growth of faults in brittle rocks." *Journal of Geophysical Research* 99, no. B9 (1994): 18159-18173.

- Rao, M.V.M., and K.P. Lakshmi., "Analysis of b-value and improved b-value emissions accompanying rock fracture." *Current Science* 89, no. 9 (2005): 1577-1582.
- Rao, M.V.M., and K.P. Lakshmi., "Amplitude distribution analysis of acoustic emissions and investigation of the development of brittle fracture in rock." *Indian Journal of Pure and Applied Physics* 44 (2006): 820-825.
- Sanyal, K., and S. Butler. "An analysis of power generation prospects from Enhanced Geothermal Systems." *Proceedings World Geothermal Conference*. Antalya, Turkey: GeothermEx, 2005.
- Sasaki, S. "Characteristics of microseismic events induced during hydraulic fracture experiments at the Hijiori hot dry rock geothermal energy site, Yamagata, Japan." *Tectonophysics* 289, no 1-3 (1998): 171-188
- Shah, K., and J. Labuz. "Damage mechanics in stressed rock from acoustic emission." *Journal of Geophysical Research* 100, no. B8 (1995): 15527-15539.
- Shigeishi, M., and M. Ohtsu. "Identification of AE sources by using SiGMA-2D moment tensor analysis." *Acoustic Emission: Standards and Technology Update*. Edited by S. Vahaviolos. Philadelphia: American Society for Testing and Materials, 1999. 174-188.
- Shiotani, T., M. Ohtsu, and K. Ikeda. "Detection and evaluation of AE waves due to rock deformation." *Construction and building materials* 15 (2001): 235-246.
- Scholz, C. "Experimental study of the fracturing process in brittle rock." *Journal of Geophysical Research* 73, no. 4 (1968): 1447-1454
- Shuck, L. Z., and T. W. Keech. "Monitoring acoustic emission from propagating fractures in petroleum reservoir rocks." Edited by H. R. Hardy and F. W. Leighton. *Proceedings first conference on acoustic emission/microseismic activity in geologic structures and materials*. University Park: Trans Tech Publications, 1975. 309-338.
- Sleefe, G.E., N.R. Warpinski, and B.P. Engler. "The use of broadband microseisms for hydraulic-fracture mapping." *SPE annual technical conference and exhibition*. Houston: Society of Petroleum Engineers, 1995. 233-239.
- Stanchits, S., S. Vinciguerra, and G. Dresen. "Ultrasonic velocities, acoustic emission characteristics and crack damage of basalt and granite." *Pure and Applied Geophysics* 163, no. 5-6 (2006): 975-994.
- Stein, S., and M. Wyss. *An introduction to seismology, earthquakes, and earth structure.*, United Kingdom (2003): Blackwell.
- Taleghani, A., and J. Lorenzo. "An alternative interpretation of microseismic events during hydraulic fracturing." *SPE Hydraulic Fracturing Technology Conference and Exhibition*. Woodlands, TX. 24-26 January, 2011. 1-11.
- Tester, J.W., et al. "The future of Geothermal Energy." Cambridge: Massachusetts Institute of Technology (2006)

- Walderhauser, F., and W. Ellsworth. "A double difference earthquake location algorithm: Method and application to the North Hayward fault, California." *Seismological Society of America* 90, no. 6 (2000): 1353 – 1368.
- Walsh, J.B., "Seismic wave attenuation in rock due to friction." *Journal of Geophysical Research* 71, no. 10 (1966): 2591-2599).
- Warpinski, N., P. Branagan, R. Peterson, S. Wolhart, and J. Uhl. "Mapping hydraulic fracture growth and geometry using microseismic event detection by a wireline retrievable accelerometer array." *The SPE Gas Technology Symposium*. Calgary, 1998. 335-346.
- Warpinski, N., Z. A. Moschovidis, C. D. Parker, and I. S. Abou-Sayed. "Comparison study of hydraulic fracture models - Test case: GRI staged field experiment No. 3 (includes associated paper 28158)." *SPE Production & Facilities* 9 No. 1 (1994): 7-16.
- Whittaker, B., B.G. Sun, R. Sigh. "Rock Mechanics: Principles, Design, and Applications." Elsevier Science
- Winterstein, D., How shear-wave properties relate to rock fractures: Simple cases." *Geophysics: The Leading Edge of Exploration* (1992): 21-28.
- Wohlenberg, J., and H. Keppler. "Monitoring and interpretation of seismic observations in hot dry rock geothermal energy systems." *Geothermics* 16, no. 4 (1987): 441-445.
- Zang, A., C. Wagner, S. Stanchits, G. Dresen, R. Anderson, and M. Haidekker. "Source analysis of acoustic emissions in Aue granite cores under symmetric and asymmetric compressive loads." *Geophysics Journal International* 135 (1988): 1113-1130.
- Zoback, M.D., F. Rummel, R. Jung, C.B. Raleigh, "Laboratory hydraulic fracturing experiments in intact and pre-fractured rock" *Int. J. Rock Mech. Min. Sci. Geomech. Abstr.* 14, no. 2 (1977): 49-58